Germanium Quantum Wells for Semiconductor Qubits

Supervisor: **Prof. Daniel Chrastina**

Candidate:

STEFANO CALCATERRA

Student ID: 928497

Academic Year 2021/2022

Contents

List of Figures

List of Tables

Sommario

Recentemente, il computer quantistico è divenuto un soggetto di ricerca di primissimo piano per la comunità scientifica mondiale. Nonostante alcuni risultati promettenti, una tipologia dominante di implementazione del qubit non si è ancora affermata.

Una realizzazione promettente è costituita da due quantum dot accoppiati, definiti elettrostaticamente in un gas bidimensionale di portatori. I principali vantaggi di tale implementazione risiederebbero nell'elevato tempo di coerenza e nell'integrazione con l'hardware attuale.

Lo scopo di questa tesi è la caratterizzazione di eterostrutture di Ge/SiGe in cui confinare il gas bidimensionale di portatori.

Le strutture sono state cresciute sfruttando la tecnica LEPECVD (Low-Energy Plasma-Enhanced Chemical Vapor Deposition) in L-NESS.

Le proprietà di trasporto del gas bidimensionale sono state analizzate a bassa temperatura (fino a 1.6 K) mediante effetto Hall classico ed effetto Hall quantistico. La massa efficace, la mobilità, la densità bidimensionale di portatori, il Dingle ratio e la densità critica sono stati estrapolati per ogni campione analizzato.

Abstract

In the last few years, quantum computing has become a major research topic for the scientific community. Despite some exciting results, there has not yet been a real breakthrough for the implementation of the qubit.

A promising realization is that formed by two coupled quantum dots, electrostatically defined in a two dimensional carrier gas. The main advantages of such a implementation are its long coherence time and its relatively straightforward integration with classical hardware.

The purpose of this master's thesis is the realization and characterization of Ge/SiGe heterostructures, in which to confine a two dimensional hole gas. Heterostructures have been grown by LEPECVD (Low-Energy Plasma-Enhanced Chemical Vapor Deposition) at L-NESS.

Transport properties of the hole gas have been analyzed at low temperature (down to 1.6 K) exploiting classical Hall effect and quantum Hall effect. Effective mass, mobility, sheet density of carriers, Dingle ratio, and critical density have been extracted for every sample studied.

Introduction

In the last few years, the research world seems to be on the verge of the so-called second quantum revolution, with the development of new quantum technologies. The most important and interesting quantum technology is the quantum computer. As the invention of the Si MOSFET led rapidly to mass production of computers, so a breakthrough technology to implement the quantum bit would open a new era of quantum computers. Several different realizations of the qubit have been proposed through the years, each with its strengths and weaknesses.

A promising implementation is that formed by two coupled quantum dots hosted in a Ge/SiGe heterostructure, realizing a quantum two-level system (logical qubit). The main advantages of this qubit would be its long coherence time and its integration with classical hardware. [1, 2, 3, 4, 5].

The purpose of this thesis is the characterization of the transport properties of the Ge/SiGe heterostructures in which a two-dimensional carrier gas (2DCG) is confined. In this case the confined carriers are holes, so it is better defined as a hole gas (2DHG).

The heterostructure studied in this thesis is the HMOS (heterostructure metal-oxide-semiconductor). The HMOS is an undoped heterostructure in which a layer of strained Ge is grown between two layers of SiGe. In order to electrostatically define quantum dots, gate structures were fabricated on LEPECVD grown HMOS at the IST (Institute of Science and Technology, Klosterneuburg, Austria) for their own qubit studies.

Hall bars fabricated at the IST featuring an aluminium oxide gate dielectric deposited by ALD (atomic layer deposition) were sent back to L-NESS for magnetotransport characterization. Moreover, some SiGe graded buffers grown at L-NESS were sent to the CAS (Chinese Academy of Sciences, Beijing, China) where the Ge quantum well stack has been grown by MBE, with isotopically pure silicon and germanium. The resulting nuclear spin-free material should enhance the spin lifetimes.

Undoped heterostructures were grown at L-NESS (Laboratory for Nanostructure Epitaxy and Spintronics on Silicon, Como, Italy) by LEPECVD (Low-Energy Plasma-Enhanced Chemical Vapor Deposition) [6].

Transport properties of 2DHGs are studied making use of the classical Hall effect and the quantum Hall effect. In order to work at cryogenic temperatures, where quantum effects are activated, and in presence of a magnetic field, a cryostat was used. The cryostat made it possible to work at temperatures down to 1.6 K and a magnetic field up to 7.5 T.

For every sample (when possible) effective mass, mobility, carrier density, Dingle ratio, and critical, or *percolation*, density have been measured. The critical density is the minimum density required to establish metallic conduction by overcoming charge carrier localization from impurities or defects. High mobility and low percolation density are signs of material uniformity and low disorder, both of which are required to produce stable quantum dots.

In the first chapter of this thesis HMOS heterostructures are studied theoretically, with a special attention to their band structure. Then transport theory is discussed, and scattering mechanisms typical of these heterostructures are presented.

In chapter two, the LEPECVD system and the cryostat are described.

The third chapter is dedicated to the explanation of classic and quantum Hall effect, highlighting how to exploit these phenomena to obtain mobility, sheet density, effective mass, Dingle ratio and critical density of a 2DHG.

In chapter four, experimental results are presented and discussed, with a particular attention to mobility, as an important requirement for the stability of quantum dots.

1 HMOS

1.1 Quantum Dots for Quantum Computing Applications

In the last few years, the quantum computing rush has started. The fundamental milestone towards large-scale quantum computing is of course the realization of stable and reliable quantum bits (qubits). Several possible quantum bit implementations have been proposed, such as NV-centers, Josephson junction qubits, and photonic qubits [1, 2, 3, 4, 5]. None of these technologies has emerged as a real breakthrough, all featuring advantages and disadvantages.

A promising implementation could be the *coupled spins* in two quantum dots which are electrostatically defined [7]. This could be a game changer in the quantum computation scenario, due to its long coherence time and its integration with classical hardware. There are two main characteristics required for this kind of qubit [8]:

1. It must have an extremely long coherence time.

2. Fast manipulation is required.

To create an electrostatically defined quantum dot, a two dimensional carrier gas (2DCG) host and depletion gates to apply confinement are needed.

The choice of the heterostructure that will host the 2DCG has a critical impact on the features of the quantum dot. The first implementation dates to 2005, when coherent manipulation of coupled electron spins in GaAs quantum dots was shown. A very short spin dephasing time, $T_2^* \sim 10$ ns, was measured, but on the other hand the manipulation time was in the order of hundreds of picoseconds [9].

Successively, the same implementation was made in silicon, in order to favour the integration with the electronics industry. ^{28}Si was used, and it led to a situation with $T_2^* \sim 120$ μs, but a manipulation time of microseconds [1].

In an attempt to find the optimal trade-off between the properties of GaAs and ^{28}Si the IST is trying to implement qubits in germanium heterostructures, since the large spin-orbit coupling allows fast manipulation [10, 11, 12,

13, 14].

In order to do this, Ge heterostructures have been grown and characterized at the L-NESS. Depletion gate structures were fabricated at the IST for their own qubit studies, while Hall bars were fabricated at the IST and sent back to the L-NESS for magnetotransport characterization. To induce a 2DHG in the Ge quantum well, a HMOS structure was realized at the IST featuring an aluminium oxide gate dielectric deposited by ALD (atomic layer deposition). For further information about manipulation of spin in quantum dots or depletion gates nanofabrication the reader is referred to ref. [15]. In Figure 1 an SEM image of a quantum dot fabricated at the IST is shown.
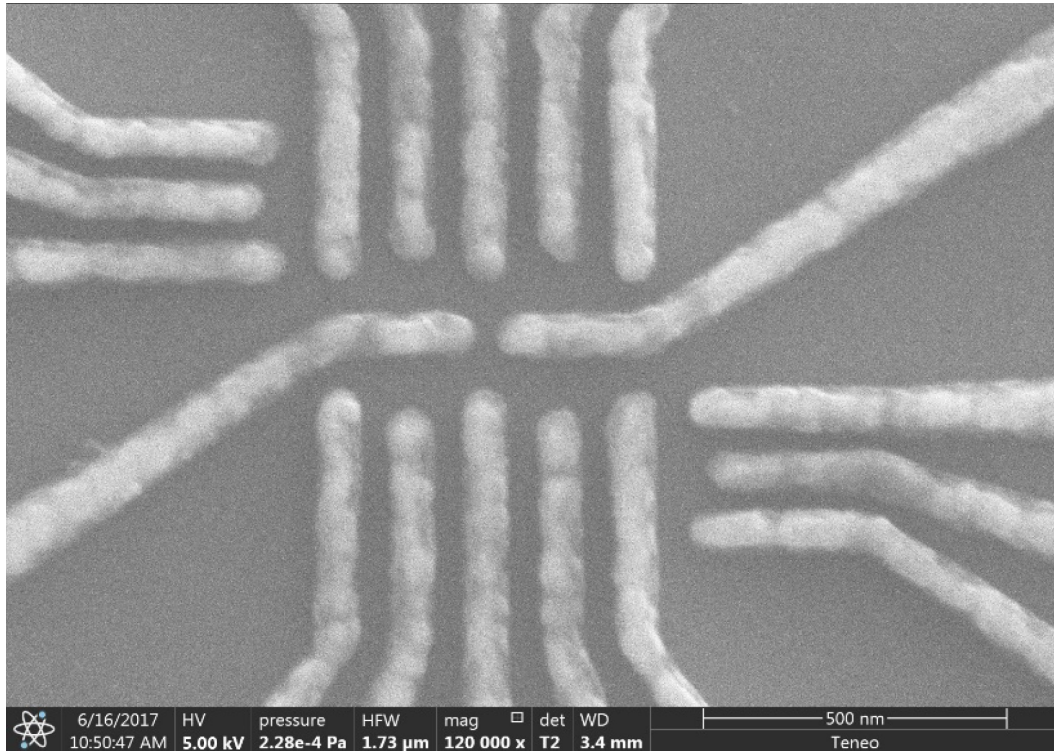
Figure 1: Top view of the gates that will confine the 2DHG in order to create a quantum dot. From IST Austria.

Like Si, Ge can be isotopically purified into a nuclear spin-free material, to achieve long spin lifetimes [13, 16]. In order to investigate this kind of material, graded buffers grown at L-NESS were sent to the CAS, where the Ge QW stack was grown by MBE, using isotopically pure Ge. Then these samples were sent back to IST and used to fabricate both qubits and Hall bars for the magnetotransport characterization at L-NESS. By investigating

the quantum transport properties of the HMOS at the L-NESS, it was possible to extract two main figures of merit: the mobility and the critical (or *percolation*) density. This latter indicates the minimum density required to establish metallic conduction by overcoming carrier trapping from impurities or defects. Large mobility and small critical density indicate material uniformity and low disorder and these are advantageous for stable and reproducible quantum dots [8].

1.2 Ge/SiGe Heterostructures

Over recent years, increasing interest has been shown in p-channel strained Ge/SiGe heterostructures, due to their large room-temperature mobility, compared to Si-based devices [17]. Numerous studies on the impact of strain and on the scattering mechanisms in modulation-doped Ge/SiGe heterostructures have allowed for a low temperature mobility increase to $\sim 1 \cdot 10^6 \frac{cm^2}{Vs}$. Modulation doping, however, introduces impurities that are a source for charge noise, gate leakage and device instability at low temperature. Therefore undoped Ge/SiGe quantum wells are preferable for quantum dot application.

Undoped Si/SiGe heterostructures have been shown to host high mobility 2D electrons, with a large density tunability [17, 18], and even higher mobility values have been reached for GaAs/AlGaAs heterostructures [19, 20]. However, these materials are not the optimal choice for qubit realization, as discussed above.

The structure of a Ge/SiGe heterostructure studied in this thesis is shown is shown in Figure 2:
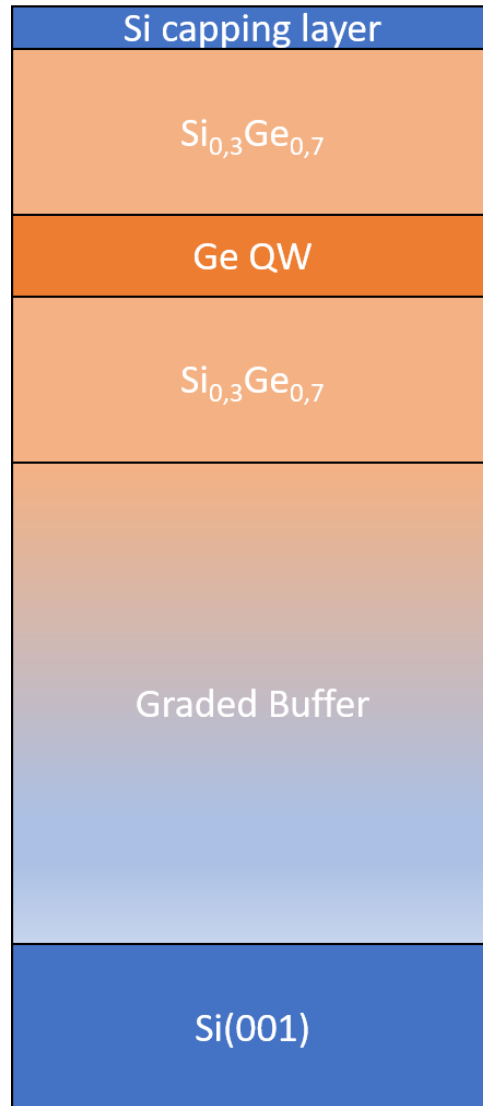
Figure 2: 10721 HMOS structure

The starting point is a lightly p-doped Si(001) wafer, on which a graded buffer is grown. A graded buffer is basically a thick layer in which the concentration of germanium has been increased by 7% each micron, so after 10 μm the final alloy composition is $Si_{0.3}Ge_{0.7}$. Then 2 μm are grown at a constant composition of $Si_{0.3}Ge_{0.7}$ to form a high-quality fully-relaxed layer [21]. The stack composed by the Si wafer and the graded buffer becomes a virtual $Si_{0.3}Ge_{0.7}$ substrate. The most important part of the HMOS is the channel, in which carriers transport takes place. The channel is 18 nm thick, and is made of nominally pure Ge. The Ge channel is then covered by a 20 nm $Si_{0.3}Ge_{0.7}$ barrier. The last layer is a 2 nm Si sacrificial cap.

Bearing in mind the lattice mismatch between $Si_{0.3}Ge_{0.7}$ and Ge, the channel is subject to compressive strain: this has consequences on the band structure and so on the effective mass, as we will discuss later.

For Ge/SiGe heterostructures, densities ranging from $\sim 1.1 \times 10^{10}\,\mathrm{cm}^{-2}$ to $\sim 1.5 \times 10^{11}\,\mathrm{cm}^{-2}$ have been achieved, with a peak mobility of $\sim 3 \times 10^5\,\mathrm{cm}^2/\mathrm{Vs}$ and an in-plane effective mass $m^* = 0.105 m_e$, for a $Si_{0.2}Ge_{0.8}$ structure with barrier hundreds of nm thick [17]. More recently, structures featuring a lighter effective mass ($m^* = 0.05 m_e$ at zero density), a large range of densities (up to $\sim 1.1 \times 10^{12}\,\mathrm{cm}^{-2}$), and $\mu > 5 \times 10^5\,\mathrm{cm}^2/\mathrm{Vs}$ have been developed [22].

1.3 Band Structure

The energy gap of Ge is smaller than that of Si so, once these materials are connected, there is a valence band offset and a conduction band offset [23]. In this specific case, a heterostructure made of a layer of pure Ge embedded in two layers of $Si_{0.3}Ge_{0.7}$ is a quantum well of the *second type*. This means that the bands will rearrange in order to confine holes in the Ge layer and to be a barrier for the electrons that tend to enter in this layer.

In the undoped situation typical of HMOS, bands do not curve until the applied gate bias causes the charge to accumulate in the channel (Figure: 3).
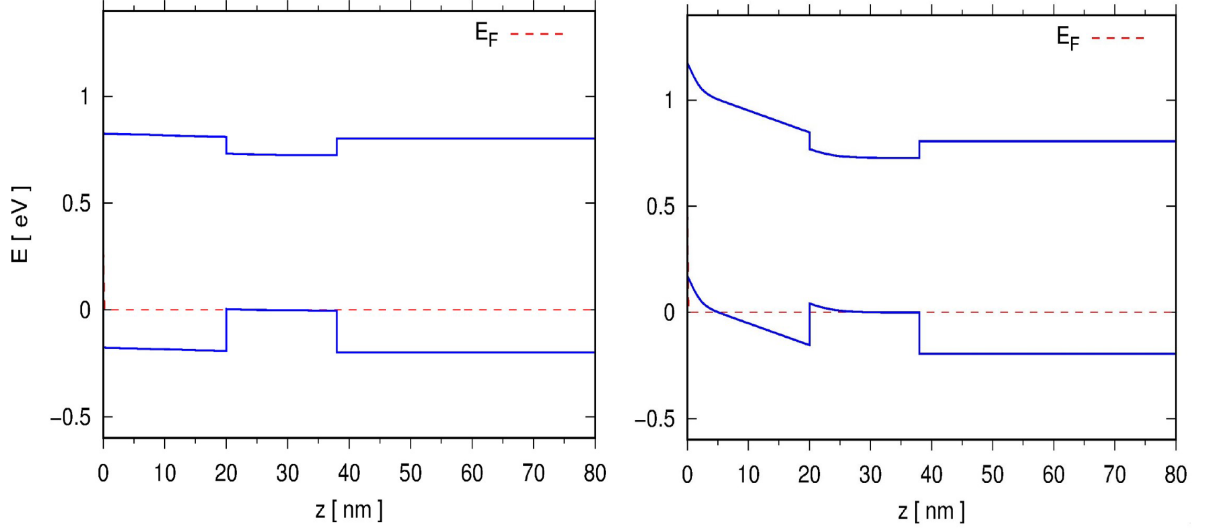
Figure 3: Band structure profile for a HMOS structure. On the left a voltage gate V_g = -0.9 V is applied, on the right V_g = -1.6 V. It is possible to observe that a more negative voltage leads to a lower energy in the channel layer and so to a higher sheet carrier density.

High bias may however lead to accumulation of charge at the surface. When bands are bent, it is energetically favorable for the holes to migrate into the Ge channel. Here they are confined along the growth direction but free to move in the plane of the wafer.

The quantum well in which holes are confined is not the well-known rectangular well, but it is better resembled by a triangular potential. The wavefunction for the lowest energy state can be approximated by the Fang-Howard wavefunction:

$$\Psi_0 = \left(\frac{b^3}{2}\right) z \exp\left(-\frac{bz}{2}\right) \tag{1.3.1}$$

where b is defined as

$$\left[\frac{12 m_z e^2}{\hbar^2 \epsilon_r \epsilon_0}\left(n_d + \frac{11}{32} n_s\right)\right]^{\frac{1}{3}} \tag{1.3.2}$$

where n_d is the density of the ionized background impurities and m_z is the effective mass in the confinement direction.

$$\psi_0(z)=\left(\frac{b^3}{2}\right)^{1/2} z \exp\left(-\frac{bz}{2}\right)$$

Fermi level

E_0 ┄┄ E_F

E_1

Ge   Si$_{1-x}$Ge$_x$

Valence Band

Growth Direction (z)

Carrier Gas in k-space (k_x,k_y)

E_0

E_F

States filled up to Fermi Level

$$k_F=\sqrt{2\pi n_s}$$

$$E=\frac{\hbar^2 k^2}{2m^*}$$
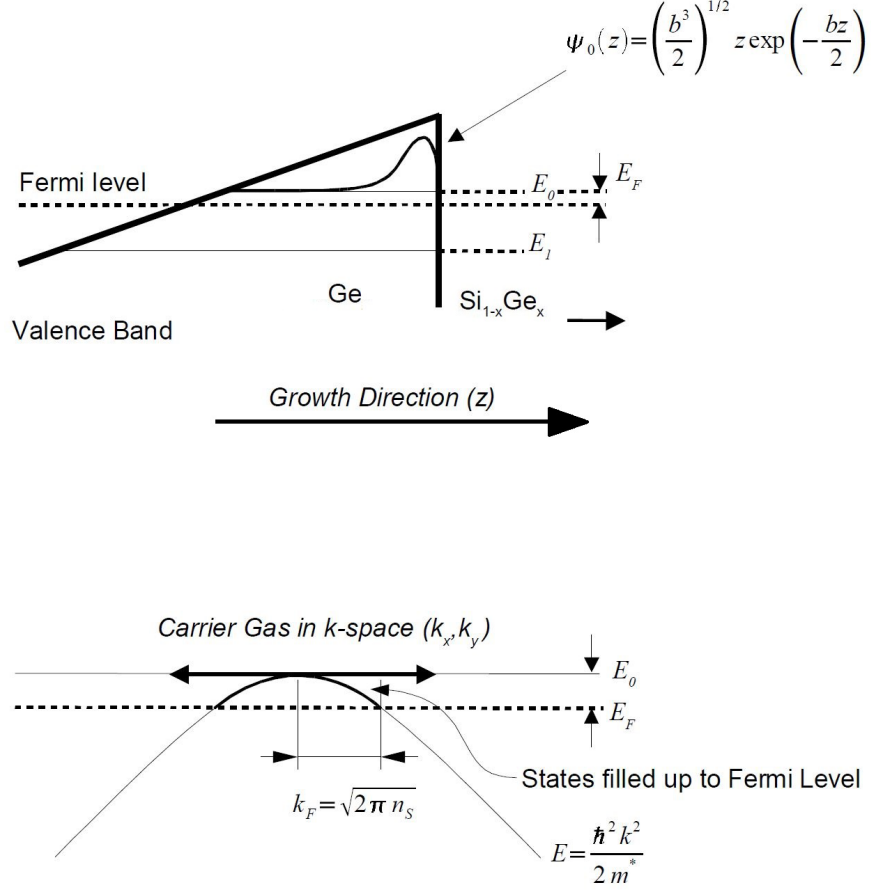
Figure 4: In the upper part there is a detail of the interface between the channel and the Si$_{0.3}$Ge$_{0.7}$ setback, where the 2DHG is confined. E_0 and E_1 represent the two lowest quantum energy levels. The lower panel shows how the Fermi Energy E_F depends on the sheet density in the simplest case of constant, isotropic effective mass [24]

1.4 Effective Mass

In bulk unstrained SiGe the light hole (LH) and heavy hole (HH) bands are degenerate at the Γ point. This degeneracy is broken by quantum well confinement, since LH is composed by p_x, p_y, and p_z orbitals instead HH only by p_x and p_y.

Considering that greater orbital overlap means greater conductivity, due to the fact that the p_z overlap is weaker than the p_x and p_y overlaps in a QW, the HH band has a heavier mass in the confinement direction and a lighter

mass in the plane of the QW. For the LH band the reverse is true. To sum up, in a quantum well, counter-intuitively:

$$m_{HH}^{*xy} < m_{LH}^{*xy} \qquad (1.4.1)$$

In HMOS studied in this thesis, confinement is not the only factor that will modify the in-plane effective mass. In fact, it has to be considered that the Ge channel is subjected to compressive strain [25]. In a qualitatively way, when Ge is compressively strained the p_x and p_y overlap is stronger since atoms are closer together in the plane, while the p_z overlap is weaker for the opposite reason. It is easy to understand that compressive strain will have the same consequence as confinement. These two effects work in a cooperative way to make the HH in-plane effective mass lighter, and so to increase mobility.

1.5 Transport Theory

The most relevant physical quantity needed to characterize the transport properties of a 2DHG is the mobility μ, which can be defined as:

$$\mu = \frac{v}{E} \qquad (1.5.1)$$

where v is the drift velocity of the carriers and E is the applied electric field. In a low-temperature Drude model, mobility can be rewritten as:

$$\mu = \frac{e\tau_{tr}}{m^*} \qquad (1.5.2)$$

in which τ_{tr} is the transport lifetime. From the previous equation it is clear that, in order to increase mobility, one must either reduce the effective mass of the carriers or increase the τ_{tr}. The total transport lifetime can be calculated with Matthiensen's rule:

$$\tau_{tr,tot}^{-1} = \sum_{i=1} \tau_i^{-1} \qquad (1.5.3)$$

This equation states that the total scattering rate is the sum of the single scattering rates, assuming all scattering mechanisms as independent [26]. The following discussion needs to introduce two main approximations:

- The Fermi surface is assumed to be circular in the conduction plane, even if the heavy hole band features a slight anisotropy [27].

- Scattering is only elastic: a hole with a wavevector $\vec{k_i}$ will scatter into a final state $\vec{k_f}$ where $|\vec{k_i}| = |\vec{k_f}| = |\vec{k_F}|$, being $\vec{k_F}$ the Fermi wavevector. This second assumption is reasonable in a low temperature regime, so that $k_B T << E_F$.

Since the modulus of the wavector is conserved, what changes is its direction (Figure 5) [28].

The modulus of the scattering vector can be calculated as:

$$|\vec{q}| = |\vec{k_f} - \vec{k_i}| = 2k_F \sin\frac{\theta}{2} \tag{1.5.4}$$

where θ is the angular variation of direction between the initial and the final wavevector.
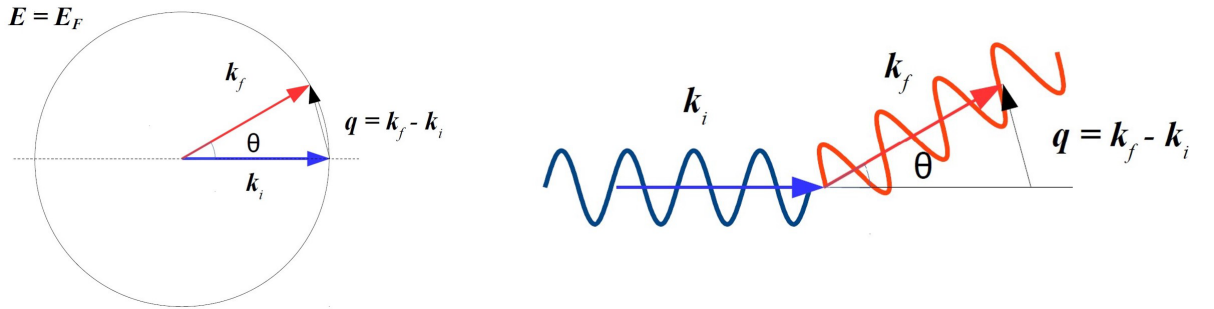
Figure 5: Schematic representation of a scattering event between two states with $|\vec{k_i}| = |\vec{k_f}| = |\vec{k_F}|$

In this framework it is possible to define the transport scattering rate:

$$\tau_{tr,i}^{-1} = \frac{m^*}{\pi\hbar^3} \int_0^\pi (1 - \cos\theta) \frac{|V_i(q)|^2}{\epsilon_q^2} d\theta \tag{1.5.5}$$

and the quantum scattering rate:

$$\tau_{q,i}^{-1} = \frac{m^*}{\pi\hbar^3} \int_0^\pi \frac{|V_i(q)|^2}{\epsilon_q^2} d\theta \qquad (1.5.6)$$

The main difference between τ_{tr} and τ_q is that in the second, all scattering events are equally weighted, while in τ_{tr}, instead, every event is weighted by the scattering angle, so the scattering events that have a final direction of propagation very far from the initial direction will have a stronger influence on τ_{tr}. This is the reason why in the mobility definition the relevant lifetime is τ_{tr}.

In equation 1.5.5 and 1.5.6 $V(q)$ is introduced, which is the scattering matrix element: every scattering mechanism has its own and they will be analysed later. Moreover, ϵ_q is present: this is the so called *static polarizability function*. ϵ_q allows screening to be considered: this is a mechanism by which the travelling electrons feel a reduced scattering potential because all other electrons present in the semiconductor polarize to screen the scattering centers. Thomas–Fermi theory proposes a possible mathematical expression of ϵ_q [29]:

$$\epsilon_q = 1 + \frac{q_s}{q} \qquad (1.5.7)$$

where

$$q_s = \frac{m^* e^2}{2\pi\varepsilon_r\varepsilon_0\hbar^2} \qquad (1.5.8)$$

A parameter of great importance in the analysis of scattering mechanisms is the Dingle ratio [30]:

$$\alpha = \frac{\tau_{tr}}{\tau_q} \qquad (1.5.9)$$

Its significance can be better understood in the following section, where scattering mechanisms will be discussed.

Remote impurity scattering, e.g, is predominant at low angle, and this leads to a Dingle ratio bigger than unity. A value of α close to unity is an indication of interface roughness scattering or local impurity scattering.

1.6 Scattering Mechanisms

The first important point is related to phonon scattering (both acoustical and optical): it can be neglected at low temperature (where low means T < 80 K [29]). At higher temperatures, instead, it is possible to fit an empirical relation

$$\mu \sim T^{-\gamma}$$

in order to determine the limiting phonon mechanism. $\gamma = 1$ is expected for acoustic phonons, while $\gamma = 2$ is considered a manifestation of optical phonon scattering [31]. At low temperature four main scattering mechanisms will be considered:

1. Local impurity scattering.

2. Remote impurity scattering.

3. Interface roughness scattering.

4. Alloy scattering.

1.6.1 Remote Impurity Scattering

Remote impurity scattering is caused by dopant atoms that are far from the channel [32], as in the case of a modulation-doped quantum well. The scattering matrix element is [33]:

$$|V_{ri}(q)|^2 = n_D \Gamma_D(q) D(q) \left(\frac{e^2}{2q\varepsilon_r\varepsilon_0} \right)^2 \qquad (1.6.1)$$

where n_D is the doping atoms sheet density, and Γ_D is defined as:

$$\Gamma_D(q) = \frac{[1 - \exp(-2qW)]\exp(-2qS)}{2qW} \qquad (1.6.2)$$

where W is the thickness of the doped region and S is the setback distance. D(q) is the correlation between doping atoms:

$$D(q) = 1 + \frac{qW - 4\sinh(qW/2)\exp(-q^2\Delta^2)}{\sinh(qW)} \qquad (1.6.3)$$

where

$$\Delta = (W/n_D)^{\frac{1}{3}} \tag{1.6.4}$$

is the random fluctuation in dopant spacing.

The meaning of the correlation function is that at low-q the potential looks more smooth, so there is less scattering, while, at high-q, scattering is enhanced by the electric dipole created by the true position of an impurity compared to its ideal perfectly correlated position.

Remote impurities scattering can be considered a small angle scattering mechanism, and its strength depends on the carrier density, because q is related to p_s through the length of $k_F = \sqrt{2\pi n_s}$.

1.6.2 Local Impurity Scattering

Local impurities are scattering centers localized at the interface between the Ge channel and the SiGe layer. These impurities come from the background doping from dopant atoms that are in the chamber and are incorporated into the deposited SiGe. Usually they tend to migrate to the channel interface, in any case their effect is strongest when they coincide with the position of the 2DHG.

The scattering matrix element is [28]:

$$|V_{li}(q)|^2 = n_i \left(\frac{e^2}{2q\varepsilon_r\varepsilon_0}\right)^2 \frac{2}{(1+q/b)^6} \tag{1.6.5}$$

p_s appears inside b parameter defined in equation 1.3.2, indicating that the 2DHG with higher density is more closely confined to the interface due to the higher electric field. However, the main dependence of local impurities scattering on sheet density comes from the length of the q vector, as before.

1.6.3 Interface Roughness Scattering

Considering a Gaussian roughness, the scattering matrix element is [28]:

$$|V_{ir}(q)|^2 = \frac{\pi\Delta^2\Lambda^2 e^4}{(\varepsilon_r\varepsilon_0)^2} \left(n_{dep} + \frac{p_s}{2}\right)^2 \exp\left(-\frac{q^2\Lambda^2}{4}\right) \tag{1.6.6}$$

16

Here Λ is the length and Δ the height of the roughness.

This type of scattering mechanism is stronger when p_s increases since a stronger field confines the carriers closer to the interface.

1.6.4 Alloy Scattering

Alloy scattering exists because even though the SiGe alloy has a crystalline structure, whether a Si or Ge atom occupies a particular lattice site is random [24]. The scattering matrix element is [34]

$$|V_x(q)|^2 = x(1-x)\Omega_0 \delta E^2 \frac{3b}{16} \tag{1.6.7}$$

where $\Omega_0 = \frac{a^3}{8}$ and is the volume occupied by one atom, δE is the strength of the interaction and b was defined in eq. 1.3.2. Alloy scattering should be negligible in pure Ge quantum wells, although x-ray diffraction results suggest that up to a few percent of Si may be present. Also, the finite barrier height at the Ge/SiGe interface means that a small probability density of the 2DHG exists within the $Si_{0.3}Ge_{0.7}$ barrier

1.7 Percolation Density

The *percolation density* is an important figure of merit to describe the so-called two-dimensional metal-insulator transition (2D-MIT). The phenomenon refers to the observation of a carrier density-induced qualitative change in the temperature dependence of the resistivity $\rho(n, T)$, where n_p is a critical density separating an effective "metallic" phase ($n > n_p$, $\frac{d\rho}{dT} > 0$) from an "insulating" phase ($n < n_p$, $\frac{d\rho}{dT} < 0$). The 2D MIT phenomenon occurs in relatively high-mobility systems, although the mobility values range from 10^4 cm^2/Vs to 10^7 cm^2/Vs, depending on the 2D system under consideration. The 2D MIT phenomenon is also considered to be a low-density phenomenon although, depending on the 2D system under consideration, the critical density differs by some orders of magnitude (e.g. $n_p \sim 10^{11}$ cm^{-2} in 2D Si and $\sim 10^9$ cm^{-2} in high-mobility GaAs/AlGaAs heterostructures). The universal features of the 2D MIT phenomenon are:

1. The existence of a critical density n_p distinguishing an effective high-density metallic phase from an effective low-density insulating phase.

2. While the insulating phase mostly manifests the conventional activated transport behavior, the metallic temperature dependence is universal, in the sense that it manifests a very strong temperature dependence, not seen in standard three-dimensional metals.

[35, 36, 37].

In order to extract the percolation density from electrical characterization measurements, the conductivity σ can be written as:

$$\sigma(n) \sim (n - n_p)^p \tag{1.7.1}$$

where p is the *percolation exponent*. Its value is theoretically predicted as 1.31. Experimentally, at very low temperatures ($T < 1$ K) the percolation exponent seems to be temperature independent, while it grows with temperature for $T > 1$ K [35].

Since the percolation density characterizes disorder at low densities, which is the typical regime for quantum dot operation, a low value of this parameter is considered a requirement for a good stability of the quantum dots. Recently, values of the order of $n_p = 2.1 \times 10^{10} \, \text{cm}^{-2}$ have been achieved in Ge/SiGe heterostructures. [38].

2 Experimental Techniques

2.1 Low-Energy Plasma-Enhanced Chemical Vapor Deposition

Two of the samples studied in this thesis have been fully grown by LEPECVD (Low-Energy Plasma-Enhanced Chemical Vapor Deposition). This relatively new technique is based on the principle of the CVD, but allows many of the problems of CVD to be overcome [6, 39]. A classical CVD has some typical growth problems. First there is an exponential dependence of the growth rate on the substrate temperature. This is a consequence of the thermal energy needed to decompose precursors, and to allow hydrogen desorption from the substrate. These conditions mean that very high temperatures are required to have a significant growth rate (>1000°C for Si). Furthermore, since Ge and Si have two very different H desorption rates, there is a strong temperature dependence of the deposition rate of the SiGe alloy and a strong non-linearity between gas composition and alloy composition [40, 41].

In LEPECVD an argon plasma is introduced into the chamber, and thanks to a magnetic field it is focused on the Si wafer which is heated with a graphite heater. The Ar plasma cracks the gaseous precursors of the materials and so the radicals deposit on the wafer. In such a way an epilayer is grown. Usually SiH_4 and GeH_4 are the precursors for SiGe growth and PH_3 and B_2H_6 (diluted in Ar) are used to introduce n and p-type dopants.
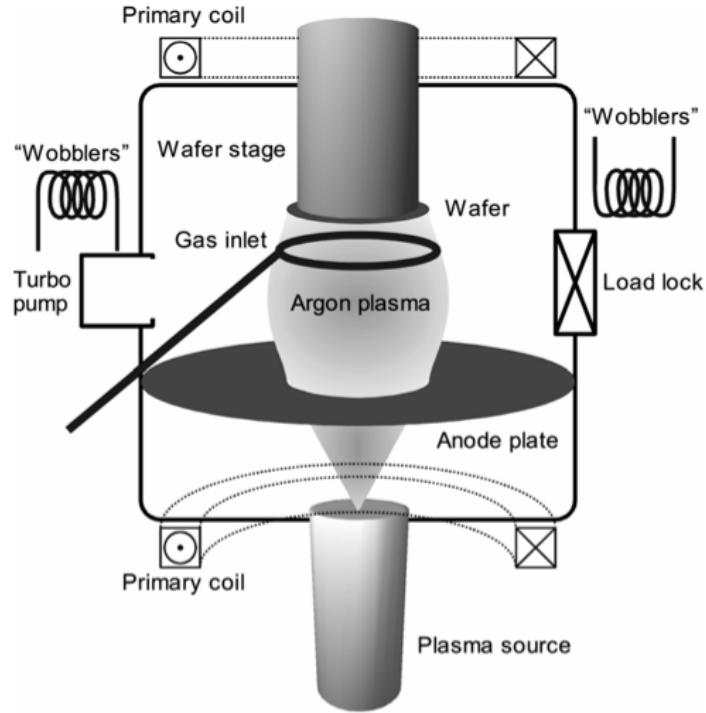
Figure 6: The low-energy plasma-enhanced chemical vapor deposition (LEPECVD) system. A low-voltage high-current DC discharge is sustained between the source and the anode plate. The substrate is exposed to the plasma, but the ion energies are too low to cause any damage [39].

LEPECVD overcomes problems mentioned above exploiting the high reactivity of the radicals and the ion bombardment, that removes hydrogen from the surface of the substrate [42]. It is important to stress that the energy of ions is around 5–10 eV, not enough to cause any damage to the crystal. So LEPECVD allows the growth of crystalline material as in thermal CVD, but with a much higher growth rate especially at low temperatures. For $Si_{1-x}Ge_x$ of any composition, the growth rate can be varied from 0.1 nm/s to almost 5–10 nm/s at substrate temperatures of 450–750°C. The growth rate depends on the precursor gas flow, on the plasma arc current, and on the magnetic confinement. These characteristics make it possible to grow both thin films with nanometer precision and several micron thick layers using the same reactor and in the same deposition process.

2.2 Cryostat

A closed-cycle He cryostat has been employed for low temperature measurements. The operation range of this machine sweeps from 1.6 to 300 K. A superconducting solenoid, kept below its critical temperature, makes it possible to generate a magnetic field for Hall measurements. The range of the generated magnetic field sweeps from -7.5 to 7.5 T.

The cooling system of the cryostat is divided into two parts. The first part is a compressor used to cool down the He pot, all the internal parts, and the solenoid to a temperature below 4.2 K. In the second part of the system there is He at roughly atmospheric pressure. It comes into contact with the inlet trap, which is cooled down below 40 K, where all the impurities condense. After that the helium condenses to liquid in the He pot. It then reaches the sample space through a narrow tube. Here, liquid He evaporates at a pressure lower than atmospheric pressure, and a temperature lower than helium evaporation temperature at atmospheric pressure, cooling down the sample to a temperature of 1.6 K. After the evaporation, He is pumped away, re-inserted into the circuit and re-condensed.

The external control of this system is based on a needle valve placed between the narrow tube and the sample space. The aperture of this valve can be modified by the operator and its status is critical. If the valve is too tightly closed, not enough He can pass, so the sample cannot be cooled down, but, on the other hand, if the valve is too wide open the He passes around the system too quickly so it has no time to re-condense.

3 Magnetic Field Effects

3.1 Conductivity Tensor

The relationship between current density and electric field in the absence of a magnetic field is simply described by Ohm's law:

$$\vec{J} = \sigma \vec{E} \tag{3.1.1}$$

where σ is a scalar and is known as *conductivity*.

The situation is slightly more complex in presence of a magnetic field, in fact, as a consequence of the Lorentz force, there is an electric field perpendicular to the initial direction of the current. To describe this situation it is not possible to rely on eq. 3.1.1 but it is necessary to replace the scalar σ with a 2×2 tensor $\bar{\bar{\sigma}}$. The generalized Ohm's law can be rewritten as

$$\vec{J} = \bar{\bar{\sigma}} \vec{E} \tag{3.1.2}$$

or

$$\begin{pmatrix} J_x \\ J_y \end{pmatrix} = \begin{pmatrix} \sigma_{xx} & \sigma_{xy} \\ \sigma_{yx} & \sigma_{yy} \end{pmatrix} \begin{pmatrix} E_x \\ E_y \end{pmatrix} \tag{3.1.3}$$

It is possible to demonstrate that the diagonal terms of $\bar{\bar{\sigma}}$ are equal, and the off-diagonal terms are opposite, so that

$$\bar{\bar{\sigma}} = \begin{pmatrix} \sigma_{xx} & \sigma_{xy} \\ -\sigma_{xy} & \sigma_{xx} \end{pmatrix} \tag{3.1.4}$$

The resistivity $\bar{\bar{\rho}}$ is a 2×2 tensor too, and it is the reciprocal of the conductivity:

$$\bar{\bar{\rho}} = \bar{\bar{\sigma}}^{-1} \tag{3.1.5}$$

or

$$\bar{\bar{\rho}} = \begin{pmatrix} \rho_{xx} & \rho_{xy} \\ -\rho_{xy} & \rho_{yy} \end{pmatrix} = \frac{1}{\sigma_{xx}^2 + \sigma_{xy}^2} \begin{pmatrix} \sigma_{xx} & \sigma_{xy} \\ -\sigma_{xy} & \sigma_{xx} \end{pmatrix} \tag{3.1.6}$$

3.2 Classical Hall Effect

One of the most important effects for studying the carrier mobility in a semiconductor is the Hall effect. Some of the most important parameters such as mobility, carrier density, effective mass, and Dingle ratio can be extracted thanks to the classical and quantum Hall effect.

The classical Hall effect can be explained only by classical electromagnetism, but some approximations have to be made. First, the energy bands are considered isotropic, furthermore scattering mechanisms do not depend on the energy, and finally, only one kind of carrier has to be considered.

To describe the classical Hall effect let us consider a two-dimensional slab with length l and width w. A potential is applied to the ends of the slab and there is a current flow. When a magnetic field is present perpendicular to the surface of the slab, the carriers feel a Lorentz force in the direction perpendicular to the one of motion:

$$\vec{F} = q\vec{v} \times \vec{B} \tag{3.2.1}$$

This leads to an accumulation of charge on the borders of the slab which results in the rise of a transverse electric field and consequently a potential:

$$V_{Hall} = wE_y \tag{3.2.2}$$

A steady state is reached when the electrostatic force is equal and opposite to the Lorentz force. It is now possible to relate V_H to the magnetic field B. Keeping in mind that the current is equal to:

$$I = n_s q v w \tag{3.2.3}$$

we can derive, with the right substitutions

$$V_H = \frac{I}{n_s q} B \tag{3.2.4}$$

The off-diagonal term of the resistivity is equal to

$$\rho_{xy} = \frac{V_H}{I} = \frac{1}{n_s q} = R_H B \qquad (3.2.5)$$

R_H is the *Hall coefficient.*

Now it is easy to relate the carrier sheet density to the Hall coefficient in the following way:

$$n_s = \frac{1}{q R_H} \qquad (3.2.6)$$

Furthermore, at low magnetic field ($\mu B << 1$) it is possible also to obtain the mobility, in fact in this approximation ρ_{xx} and σ_{xx} are inversely proportional. Given $\sigma_{xx} = nq\mu$, the mobility is:

$$\mu = \frac{R_H}{\rho_{xx}} \qquad (3.2.7)$$

Considering equations 3.2.6 and 3.2.7 it is possible to understand the importance of Hall effect: thanks to it two important figures of merit are obtained. An important consideration regarding the value of carrier density is that the value obtained from eq. 3.2.6 is not valid if the approximations made at the beginning of this chapter are not respected. For this reason we will call the mobility and carrier density obtained through classical Hall effect analysis *Hall mobility μ_H* and *Hall carrier density n_H*. In the next chapter the effects of the non-idealities are treated.

3.3 Generalized Classical Hall Effect

In the last section classical Hall effect was introduced, and was proven that, considering three important approximations, the Hall coefficient R_H and the resistivity ρ_{xx} are independent of the magnetic field. In this section the generalized classical Hall effect is presented. The aim is to understand what happens when the approximations are no longer valid, so when

- There are parallel conduction channels.

- The effective mass is non-isotropic.

- The scattering events are dependent on the energy.

At the end of this section particular attention will be given to understand how the discussed theory is related to the measurements presented in this thesis work.

The elements of the $\bar{\bar{\sigma}}$ tensor will be rewritten [43] as:

$$\sigma_{xx} = \int_{-\infty}^{+\infty} \frac{s(\mu)}{(1 + \mu^2 B^2)} d\mu \tag{3.3.1}$$

and

$$\sigma_{xy} = \int_{-\infty}^{+\infty} \frac{\mu B s(\mu)}{(1 + \mu^2 B^2)} d\mu \tag{3.3.2}$$

We have introduced $s(\mu)$:

$$s(\mu) = n_s(\mu) q \mu \tag{3.3.3}$$

defined as the *generalized conductivity*, and $n_s(\mu)$, defined as the *mobility spectrum*. Eq. 3.3.1 and eq. 3.3.2 are valid only under the fundamental hypothesis that $s(\mu)$ is independent of the magnetic field.
To recover the "classical" behaviour discussed in the previous section, one has to consider the case of a δ-like mobility spectrum:

$$s(\mu) = n_0 \delta(\mu - \mu_0) e \mu \tag{3.3.4}$$

This means that only a single carrier population with mobility μ_0 is present. Combining eq. 3.3.1 and eq. 3.3.2 with 3.3.4, 3.2.5 and 3.2.7 are obtained.
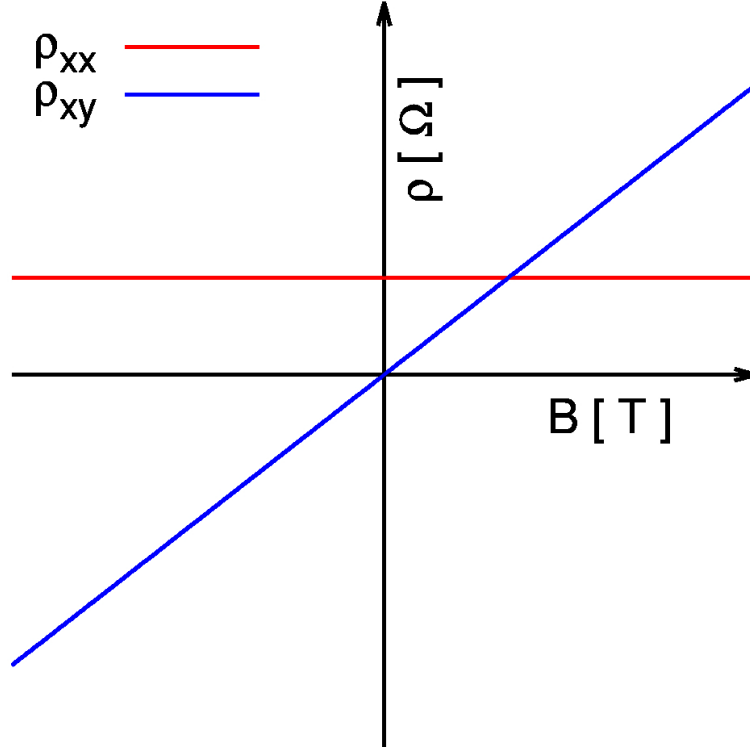
Figure 7: Qualitative plot of ρ_{xx} and ρ_{xy} when a single type carrier is present

Now we consider what happens when there is no longer a single carrier, which can happen both when more than one sub-band is occupied, or when there are parallel conduction channels (e.g. a surface channel). To model this situation each channel is treated as a δ-peak in the mobility spectrum; to keep things simple only the situation of two parallel channels is considered:

$$s(\mu) = s_1(\mu) + s_2(\mu) = n_1\delta(\mu - \mu_1)e\mu + n_2\delta(\mu - \mu_2)e\mu \qquad (3.3.5)$$

so

$$\sigma_{xx}(B) = \frac{n_1e\mu_1}{1 + (\mu_1 B)^2} + \frac{n_2e\mu_2}{1 + (\mu_2 B)^2} \qquad (3.3.6)$$

and

$$\sigma_{xy}(B) = \frac{n_1e\mu_1^2 B}{1 + (\mu_1 B)^2} + \frac{n_2e\mu_2^2 B}{1 + (\mu_2 B)^2} \qquad (3.3.7)$$

Now it is clear that R_H is no longer constant with the magnetic field, but in a low-field regime ($\mu B << 1$)

$$R_H = \frac{\pm n_1\mu_1^2 \pm n_2\mu_2^2}{q(n_1\mu_1 + n_2\mu_2)^2} \qquad (3.3.8)$$

26

On the contrary, in a high-field regime ($\mu B >> 1$)

$$R_H = \frac{1}{q(\pm n_1 \pm n_2)} \qquad (3.3.9)$$

It must be taken into account the possibility that even a single carrier gas shows a magnetoresistance, due to the fact that the scattering mechanisms are energy dependent. In order to take into account this phenomena we introduce the *scattering coefficient*:

$$r = \frac{<\tau^2>}{<\tau>^2} \qquad (3.3.10)$$

where τ is the average scattering time, and the average is made over energy. The scattering coefficient is particularly useful to take into account that R_H changes at low field in presence of an energy dependent scattering mechanism

$$R_H = \frac{r}{n_s q} \qquad (3.3.11)$$
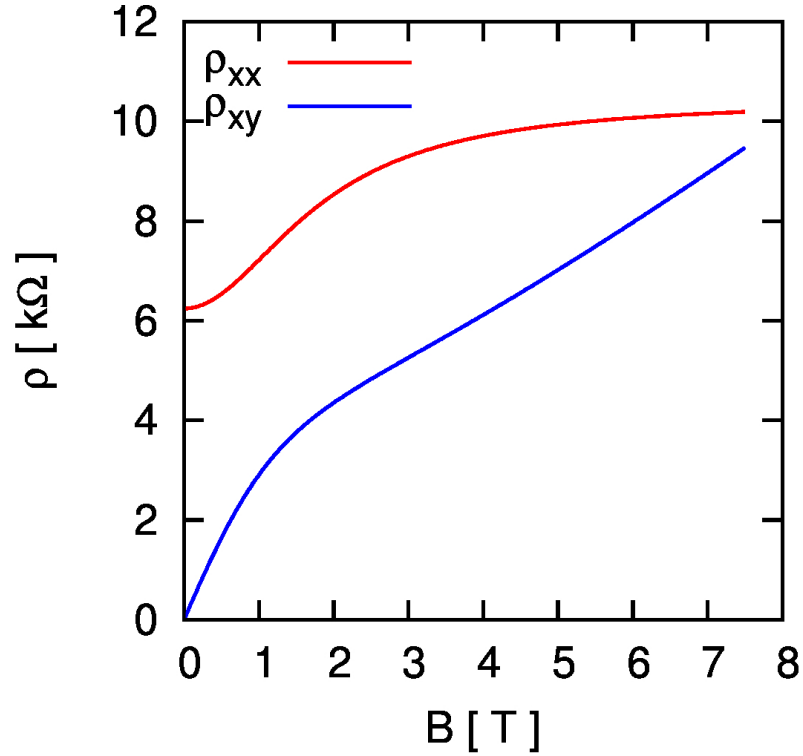
Figure 8: ρ_{xx} and ρ_{xy} in presence of two parallel channels ($n_1 = 5 \times 10^{11}$ cm^{-2}, $n_2 = 0.5 \times 10^{11}$ cm^{-2}, $\mu_1 = 1000$ cm^2/Vs, $\mu_2 = 10000$ cm^2/Vs.

At high field the Hall coefficient depends only on the total charge density in the system, so equation 3.2.5 is valid.

r theoretically considers also the anisotropy of the energy bands, which should lead to a situation in which $r < 1$ if no other effects are present [43, 44]. Actually this effect has not yet been clearly observed. It is important to stress that experimentally all these effects are indistinguishably mixed, and all contribute to the appearance of magnetoresistance.

In this thesis most of measurements were conducted at low temperature, $T < 2$ K: in this regime theoretically other parallel channel are frozen so only the holes in the quantum well give rise to the current. Furthermore, at this kind of temperature the Fermi–Dirac function can be approximated by a step function and consequently $r = 1$, so equations 3.2.5 and 3.2.6 are considered valid. The analysis that were conducted at high temperature clearly show a magnetoresistance. To study these cases, especially to investigate the presence of parallel channels, mobility spectrum analysis, discussed in the following section, has been performed.

3.4 Mobility Spectrum Analysis

In order to study the presence of parallel channels it is possible to compute the mobility spectrum $n_s\mu$ starting from the measurements of ρ_{xx} and ρ_{xy}, but to do this an inverse integral transformation has to be performed numerically. Theoretically, this can be made only if all the values of $\sigma_{xx}(B)$ and $\sigma_{xy}(B)$ from $-\infty$ to $+\infty$ are known, and of course this is a condition impossible to achieve. To attain the mobility spectrum, a numerical method by Chrastina *et al.* is used [45]. This implements the maximum entropy method through the Bryan's algorithm. Basically if two solutions are equally valid (e.g. in the way in which they fit at the least square of the original data), then the solution with the maximum entropy is preferable since it is the less compromising towards missing data. This means that the maximum entropy solution is the one that would undergo the smallest variation in presence

of new data-points. The entropy S of a discrete mobility spectrum can be defined as

$$S\{s_j\} = -\sum_{j=1}^{n} p_j \ln(p_j) \tag{3.4.1}$$

where

$$p_j = \frac{s_j}{\sigma_0} \tag{3.4.2}$$

is the probability of finding a carrier at the jth point in the discrete mobility spectrum s_j, and σ_0 is the conductivity at zero field.

Fitting of experimental points of the longitudinal and transverse conductivity becomes the problem of minimization of the Q function:

$$Q = \chi^2 - \alpha S \tag{3.4.3}$$

where

$$\chi^2 = \sum_i \frac{[\sigma(B_i) - \sigma_c(B_i)]^2}{\delta_i^2} \tag{3.4.4}$$

σ_c is the magnetoconductivity calculated from the candidate mobility spectrum, δ^2 is the error in the data measurement and α gives the relative weight of the least squares fitting and of the entropy. Bryan's algorithm weights the calculated output spectrum according to the most probable values of α [24, 45].

One interesting note is that equation 3.4.3 is quite similar to Helmholtz free energy equation

$$F = E - TS \tag{3.4.5}$$

Minimizing 3.4.5 implies minimizing the energy and maximizing the entropy. Note that in eq. 3.4.4 $\sigma(B)$ is equal to

$$\sigma(B) = \sigma_{xx}(B) + \sigma_{xy}(B) = \int_{-\infty}^{+\infty} \frac{1 + \mu B}{1 + \mu^2 B^2} s(\mu) d\mu \tag{3.4.6}$$

3.5 Quantum Treatment

At low temperature and high magnetic field, it is possible to observe some particular phenomena that are macroscopic manifestations of the quantum mechanical behaviour of the system. This kind of effects are not only interesting from a theoretical point of view but they turn out to be a powerful probe to study carrier properties and extract carrier parameters, such as the effective mass and the Dingle ratio, two figures of merit that are not found by the classical Hall effect. In order to explain this kind of phenomenon a fully quantum mechanical treatment is needed. The starting point is the time-independent Schrödinger equation that in its most general form is:

$$\left[\frac{\hat{\vec{p}}}{2m} + V(\vec{R}) \right] \Psi(\vec{R}) = E\Psi(\vec{R}) \tag{3.5.1}$$

$V(\vec{R})$ is the potential well confining the 2DHG in the channel along the z direction, so it can be rewritten as $V(z)$. Considering the applied magnetic field parallel to the z direction, it can be rewritten as $\vec{B} = (0, 0, B)$. In order to include the magnetic field in the Schrodinger equation, we define the vector potential $\vec{A}$ as

$$\vec{B} = \vec{\nabla} \times \vec{A} \tag{3.5.2}$$

The choice of $\vec{A}$ is not unique, in fact adding the gradient of a scalar potential $\vec{\nabla}(\phi)$ will not change $\vec{B}$.

The most suitable choice to deal with the described system is the so called *Landau gauge* in which $\vec{A} = (0, Bx, 0)$.

The Schrödinger equation can now be rewritten as

$$\left\{ \frac{1}{2m} \left[-\hbar^2 \frac{\partial^2}{\partial x^2} + \left(-i\hbar \frac{\partial}{\partial y} + eBx \right)^2 - \hbar^2 \frac{\partial^2}{\partial z^2} \right] + V(z) \right\} \Psi(\vec{R}) = E\Psi \vec{R} \tag{3.5.3}$$

Solving the computations:

$$\left[-\frac{\hbar^2}{2m} \nabla^2 - \frac{ie\hbar x}{m} \frac{\partial}{\partial y} + \frac{(eBx)^2}{2m} + V(z) \right] \Psi(\vec{R}) = E\Psi \vec{R} \tag{3.5.4}$$

This means that a parabolic magnetic potential appears.

It is possible to use separation of variables in order to isolate the z-dependence from the (x,y)-dependence. Furthermore, the vector potential does not depend on y. We write the wave function as a product of a plane wave that depends only on y multiplied by a function in x [29]. Substituting $u(x)\exp(iky)$ inside eq. 3.5.4:

$$\left[-\frac{\hbar^2}{2m}\frac{d^2}{dx^2} + \frac{1}{2}m\omega_c^2\left(x + \frac{\hbar k}{eB}\right)^2\right]u(x) = \varepsilon u(x) \qquad (3.5.5)$$

where one can easily recognize the one-dimensional harmonic oscillator Schrödinger equation. The frequency of the harmonic oscillator corresponds to the classical cyclotron frequency:

$$\omega_c = \frac{eB}{m} \qquad (3.5.6)$$

The main difference with respect to a classical one-dimensional harmonic oscillator is that the parabolic potential is shifted, centered in

$$x_k = -\frac{\hbar k}{eB} = -kl_b^2 \qquad (3.5.7)$$

where

$$l_b = \sqrt{\frac{\hbar}{eB}} \qquad (3.5.8)$$

is the magnetic length that can be classicaly interpreted as the size of the cyclotron orbit, while in quantum mechanics it can be regarded as the characteristic length of the wavefunction.

It is important stress that the shift of the parabolic potential is determined by the y component of the momentum [46]. The eigenvalues of the energy are

$$\varepsilon_n = \left(n + \frac{1}{2}\right)\hbar\omega_c \qquad (3.5.9)$$

associated with eigenfunctions for motion in (x,y) plane:

$$\Psi_{nk}(x,y) \propto H_{n-1}\left(\frac{x - x_k}{l_b}\right)\exp\left[-\frac{(x - x_k)^2}{2l_b^2}\right]\exp(iky) \qquad (3.5.10)$$

H_n are Hermite polynomials of order n. The wave functions look like parallel strips, extended in the y-direction, spaced equally along the x-direction, and exponentially localized around $x_k = -kl_b^2$.

Instead of a wave function that depends on two quantum numbers n and k, the energy values depend only on n and they are degenerate in k. The main consequence of the presence of a magnetic field is that the constant density of states collapses into a series of δ-functions called *Landau levels* (Figure: 9).
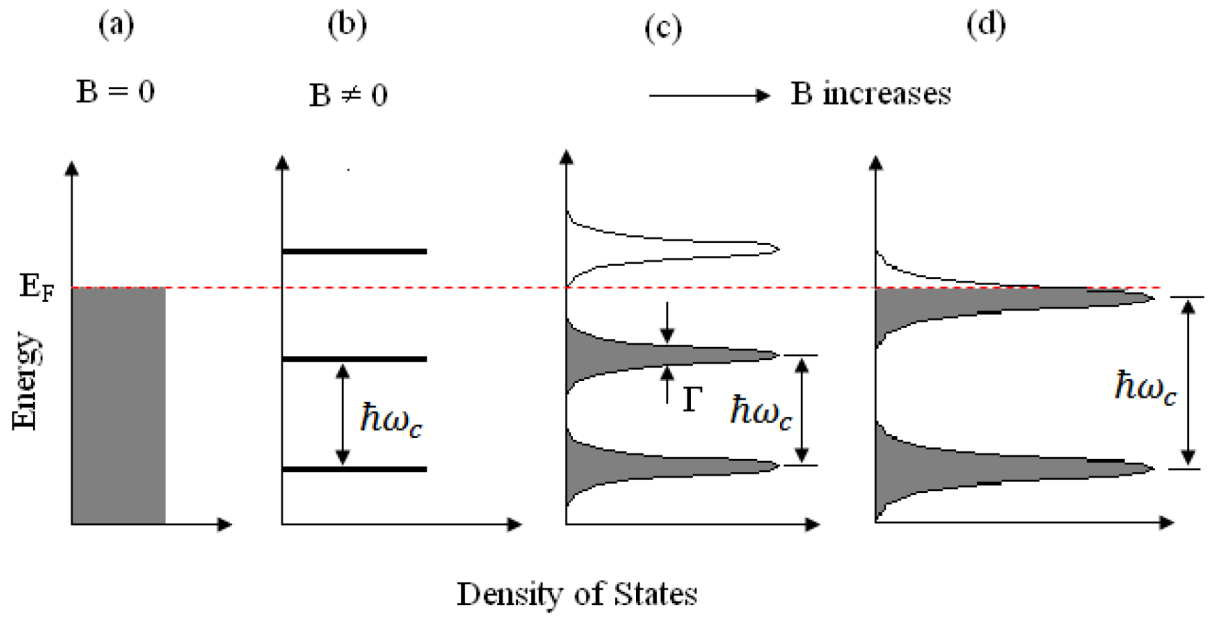
Figure 9: Density of states of 2DEG: (a) at B = 0; (b) in presence of ideal Landau levels; (c) and (d) in presence of scattering broadened Landau levels [47]

The number of states must be conserved during the condensation, so the degeneracy of a Landau level is:

$$N_L = \hbar\omega_c D_0 \tag{3.5.11}$$

where

$$D_0 = \frac{m^*}{2\pi\hbar^2} \tag{3.5.12}$$

is the density of states when no magnetic field is applied.

The degeneracy can be rewritten as

$$N_L = \frac{eB}{h} \tag{3.5.13}$$

As stated before, ideal Landau levels are δ-functions, but in reality electrons undergo scattering events that broaden the levels. The interval of time between two scattering events is τ_q and is called the quantum lifetime (eq. 1.5.6). This is not the scattering time which appears in the expression of mobility, as explained in the previous section. In literature [29] a common assumption is to consider a Gaussian or Lorentzian profile with the full width at half-maximum (FWHM)

$$\Gamma = \frac{\hbar}{2\tau_q} \tag{3.5.14}$$

Equation 3.5.14 gives the precision with which it is possible to define the energy of Landau levels. The Landau levels are resolved only when

$$\hbar\omega_c < \Gamma \tag{3.5.15}$$

or alternatively

$$\omega_c \tau_q > 1 \tag{3.5.16}$$

This implies that a carrier has to complete, without scattering events, at least one cyclotron orbit.

3.6 Shubnikov–de Haas Effect

The Shubnikov–de Haas (SdH) effect is the oscillation of the longitudinal resistivity ρ_{xx} when an applied magnetic field is increased; at high fields the oscillations can be so wide that zeros in longitudinal resistance can be observed and the quantum Hall effect develops.

3.7 Quantum Hall Effect

An increase of magnetic field leads to a bigger separation between the Landau levels (Figure 9 (c), (d)).

At a certain magnetic field, a Landau level will cross the Fermi energy E_F, so the level is emptied, and the corresponding electrons occupy the lower Landau level. It is possible to define the filling factor (number of occupied Landau levels) ν:

$$\nu = \frac{n_{2D}}{n_B} \tag{3.7.1}$$

An increasing magnetic field will raise the degree of degeneracy and decrease the filling factor.

It is possible to start to understand the reason for the oscillating behaviour of the conductivity since the longitudinal conduction depends on the density of states at the Fermi level. Nevertheless to have an (almost) complete view of this phenomena a more profound consideration of the transport in a 2DCG in presence of magnetic field is necessary [48]. When a magnetic field is applied, electrons in the bulk regions perform circular motions (cyclotronic orbits). However, this is not true for the electrons near the boundaries. In a classical view an electron tries to perform a cyclotronic orbit, but it is reflected by the boundary of the sample, and this gives rise to a *skipping* orbit. In a quantum view the boundaries of the sample add a confining potential in the Schrodinger equation

$$\left[-\frac{\hbar^2}{2m}\frac{d^2}{dx^2} + \frac{1}{2}\omega_c^2(x - x_k)^2 + V(x) \right] u(x) = \varepsilon u(x) \tag{3.7.2}$$

To model the confinement it is possible to consider $V(x) = 0$ inside the sample and an infinite potential outside. For electrons in $k = 0$ (at the center of the sample) the potential is close to parabolic, so the energy levels corresponds to the Landau levels described in equation 3.5.9. At the boundaries, for electrons with higher k, the confinement is stronger, and leads to an increase of the energy. These states are called *edge states*.
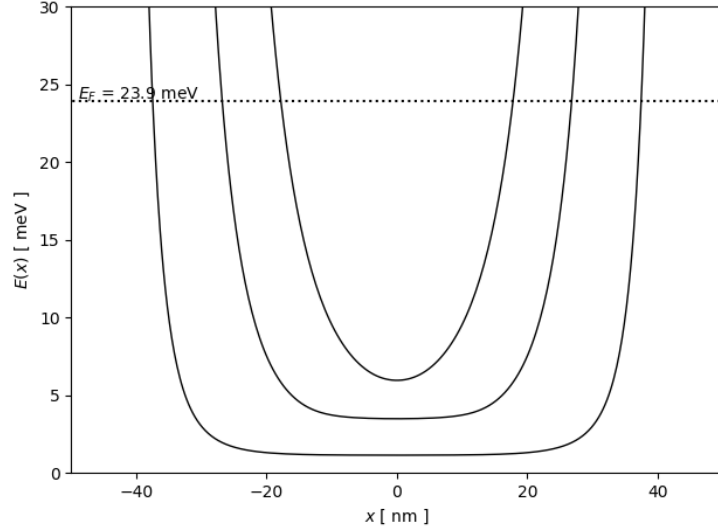
Figure 10: Bending of the states energy in function of the position: the states are higher in energy if closer to the edge

As depicted in Figure 10, the energy of the edge states will bend near boundaries, and eventually cross the Fermi level, even if the corresponding Landau level inside the sample is very far from E_F. An important property of the edge states is that the transport in an edge state is *ballistic*. This means that when a carrier is scattered, the only possible final state coincides with the initial one. In fact, once an edge state is chosen, also the corresponding k is fixed. If a forward-moving state wants to scatter into a backward-moving state it has to cross the entire sample, this means that scattering in the edge states is suppressed [49]. Electrons within the edge-channel are all at the same potential.

To observe the quantum Hall effect the voltage is measured along the sample: when the Landau levels are far from the Fermi level (few $k_B T$ below E_F) the transport is promoted only by edge channels and so it is ballistic and no voltage drop occurs. When a Landau level in the interior of the channel comes closer to the Fermi level it allows scattering events between the forward-moving electrons and the backward-moving electrons, thus a resistance between the two longitudinal contact is found.

When $\omega_c \tau_q < 1$ and the Landau levels are not so well resolved, there is always

a Landau level near the Fermi level and the changing of the magnetic field will induce Shubnikov–de Haas oscillations in the resistance instead.

3.7.1 Spin-Splitting of Landau Levels

The discussion above neglected completely the spin of the electrons. In reality, since a magnetic moment is associated with the spin it has to be taken into account when a magnetic field is applied. The magnetic moment associated with the spin can align parallel or anti-parallel to the magnetic field and these two states have different energy according to the Zeeman energy splitting.

$$E_Z = \pm \frac{1}{2} g \mu_B B \tag{3.7.3}$$

Here, the g-factor is equal to 2 for free electrons, and can assume different values inside the material due to spin-orbit coupling.

$$\mu_B = \frac{e\hbar}{2m_0} \tag{3.7.4}$$

is the well-known Bohr magneton.

At low field the Landau levels contain both spin states. The spin splitting of the Landau levels can be observed at a field high enough to satisfy the condition

$$g \mu_B B > \Gamma \tag{3.7.5}$$

3.8 Shubnikov–de Haas Oscillation Analysis

Shubnikov–de Haas oscillations are a very powerful instrument to study important parameters of a 2DCG.

First, SdH oscillations are periodic with respect to the inverse of magnetic field and the period is proportional to carrier sheet density:

$$n_s = \frac{q}{\pi \hbar \Delta(1/B)} \tag{3.8.1}$$

The calculated n_{SdH} can be compared to the more approximated n_H, being closer to the true carrier density.

Furthermore, it is possible to find the in-plane effective mass m^* and the Dingle ratio α. The resistivity of a 2DCG in a magnetic field can be modelled as [30, 50]:

$$\rho_{xx}(B,T) = \rho_0(T)\left[1 + 4\sum_{s=1}^{\infty}\frac{s\xi(B,T)}{\sinh[s\xi(B,T)]}\cdot\right.$$
$$\left.\cdot \exp\left(-\frac{\pi\alpha s}{B\mu(T)}\cdot\cos\left(2s\pi^2\frac{\hbar n_s}{qB} - \pi s\right)\right)\right] \tag{3.8.2}$$

where

$$\xi(B,T) = \frac{2\pi^2 k_B T m^*}{eB\hbar} \tag{3.8.3}$$

and

$$\alpha = \frac{\tau_{tr}}{\tau_q} \tag{3.8.4}$$

is the Dingle ratio. The main assumption behind this equation is that Landau levels become Lorentzian due to a finite lifetime τ_q. To extract m^* the temperature dependence of the oscillations is studied [51]. In the magnetic field range considered in this thesis the oscillations can be modelled considering only the s = 1 term. At any peak the cosine term becomes unity. Taking the logarithm, eq. 3.8.2 reduces to

$$\ln\left(\frac{A}{T}\right) = C - \ln(\sinh(\xi)) \tag{3.8.5}$$

where

$$A = \frac{\Delta\rho_{xx}}{\rho_0} \tag{3.8.6}$$

and C is a constant. So in order to extract m^* first a magnetic field value was chosen, corresponding to a maximum of the oscillations. Then ln(A/T) vs. T is plotted, and through a fitting, using as a fitting function eq. 3.8.5, the *in-plane* effective mass is obtained. This kind of analysis assumes that n_s does not change at low temperature, otherwise also the position of maximum

would change with the temperature. Once the effective mass is known the Dingle ratio is obtained from the so called *Dingle plot*

$$\ln\left[\Delta\rho_{xx}\frac{\sinh(\xi)}{\xi}\right] \quad \text{vs.} \quad \frac{1}{B} \tag{3.8.7}$$

where the slope is equal to $-\frac{\pi\alpha}{\mu}$.

4 Samples Characterization

4.1 LEPECVD Samples

4.1.1 Sample 10721

Sample 10721 is a HMOS grown at the L-NESS. It is composed by an undoped 18 nm thick Ge quantum well, grown on top of 2 μm of 70% graded SiGe, and covered with a 20 nm cap of 70% SiGe, on top of which there is another 2 nm Si cap. The growth temperature was 350°C, in order to achieve a flat surface on the scale of hundreds of nanometers. The top gate, used during transport characterization, is made by depositing $\sim$ 20 nm of Al_2O_3 by ALD, and then Ti/Pd as a metallic contact. The thickness of the oxide is critical: a thick oxide layer would reduce the influence of the metallic gate on the carriers, but, on the other hand, if the oxide is too thin there is a risk of oxide breakdown.

The gate voltage must be considered an additional degree of freedom, so, in principle, at each gate voltage the analysis of n_s, μ, α and m^* should be performed. Practically, this was done only for Hall 2D density and Hall mobility. For the Dingle ratio, it would have been interesting to have some points at different carrier densities, especially to check the veracity of the mobility analysis according to the 2D density, but oxide breakdown and leakage have been serious issues, often impeding this kind of measurements. In literature m^* is often approximated as constant with respect to the gate voltage, even if it is known that it has a systematic dependence on n_s in Ge/SiGe heterostructures. In this thesis work the effective mass has been extracted every time the Shubnikov–de Haas oscillations analysis was possible. Due to the difficulties mentioned above, sometimes only one value for m^* was available, and this was assumed as constant [52]. Unfortunately both the gated 10721 HMOS showed immediate oxide breakdown, making it impossible to carry out complete measurements on them.

HF cleaning   First, two devices without any oxide and top gate deposited were measured. The main difference between the two is that one of them has been treated with HF and immediately sealed, in order to clean its surface. The HF cleaning is performed to eliminate a possible boron airborne contamination, which can unintentionally introduce a p-doping in the sample [53]. This test was planned after a SIMS (Secondary Ions Mass Spectroscopy) analysis highlighted the presence of boron at the surface. Another important piece of information coming from SIMS is the presence of a relevant oxygen concentration inside the sample.
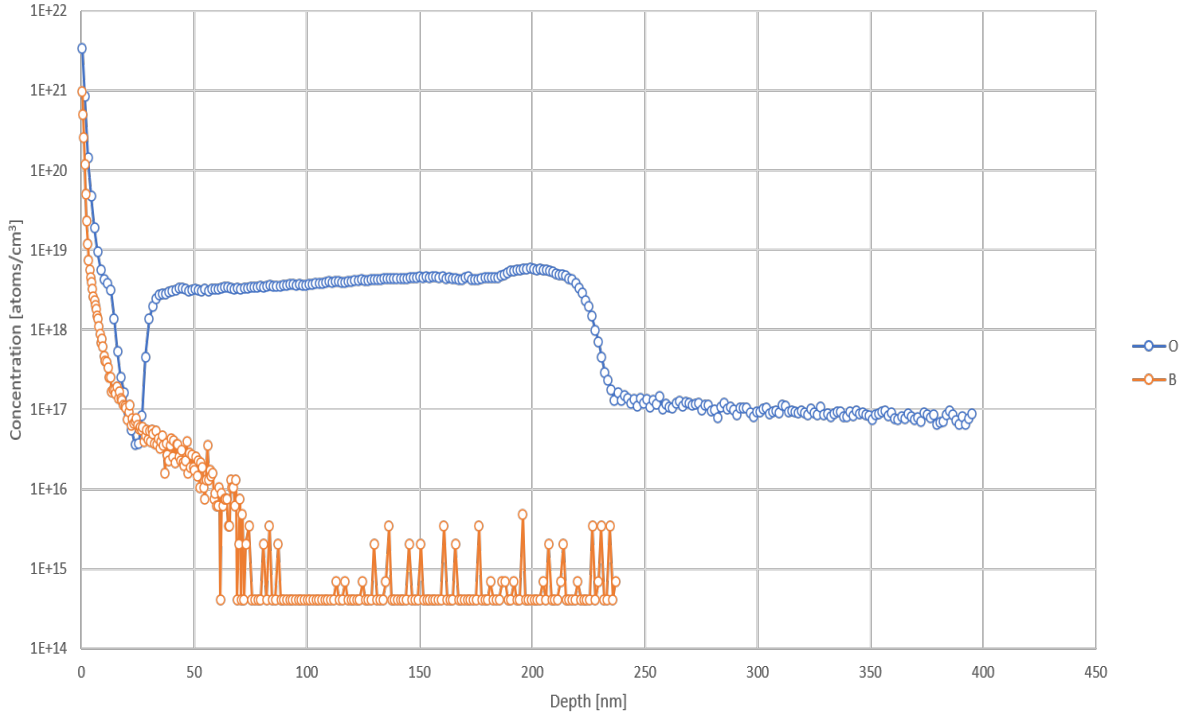
Figure 11: Concentration profile in function of depth of oxygen and boron on sample 10667, a structure nominally identical to 10721. Data are extracted from a complete SIMS analysis performed on 10667.

Oxygen contamination is known to be a limiting factor for mobility in un-doped Ge/SiGe heterostructures [13, 54]. In order to extract the Hall density and Hall mobility ρ_{xx} and ρ_{xy} have been measured at $T = 1.6$ K, sweeping the magnetic field from -0.5 to 0.5 T. In Figure 12, the graphical result of one of these measurements is shown:
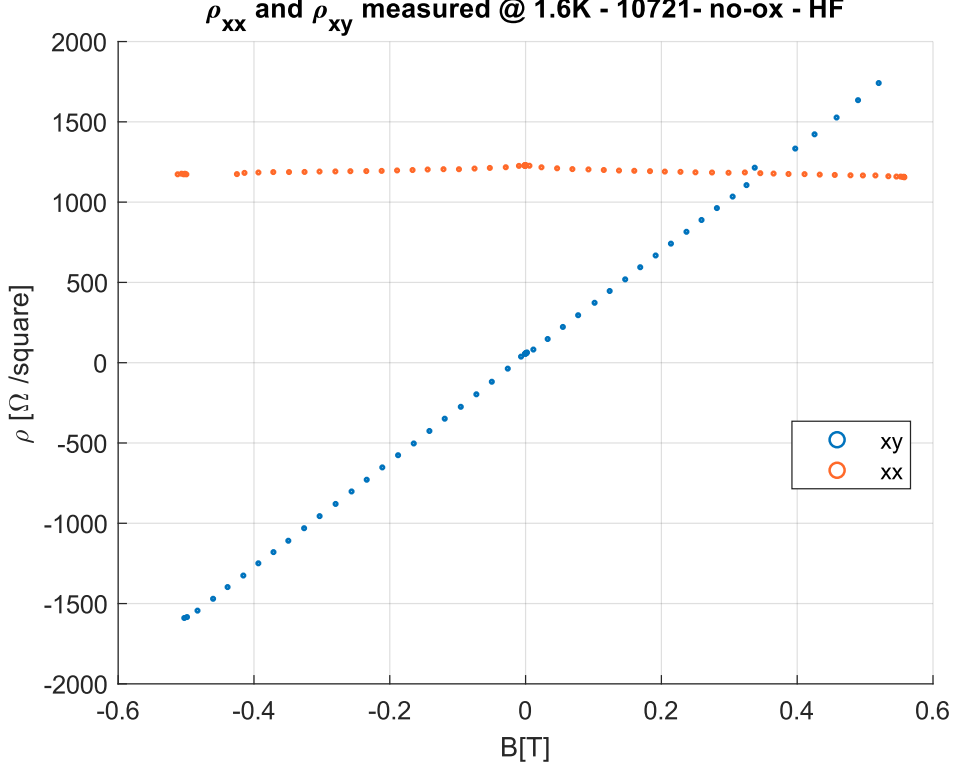
Figure 12: ρ_{xx} and ρ_{xy} data points measured at $T = 1.6$ K, sweeping the magnetic field from -0.5 to 0.5 T. The constant behaviour of ρ_{xx} and the linear behaviour of ρ_{xy} are in good agreement with theory. Compare with the qualitative plot of Figure 7.

The extracted values are shown in Table 1:

	HF treated	Not treated
μ [cm^2/Vs]	2.61×10^4	5.38×10^4
p [cm^{-2}]	1.90×10^{11}	3.16×10^{11}

Table 1: Results of Hall measurements on 10721 without top gate and oxide.

These results show that, even if carrier density is lower after the HF cleaning, the device is still working at 1.6 K, with a carrier density of the order of 10^{11} cm^{-2}. This means that the growth introduces a p-type background. However, all the other devices analyzed in this thesis have been cleaned with HF.

QHE on HF cleaned sample The relatively low density of these two samples prevented a Shubnikov–de Haas oscillation analysis, even though it was pos-

sible to measure the quantum Hall effect, sweeping the field from 0 to 7.5 T. In Figure 13 ρ_{xx} and ρ_{xy} of the HF treated sample are plotted as a function of the applied magnetic field.
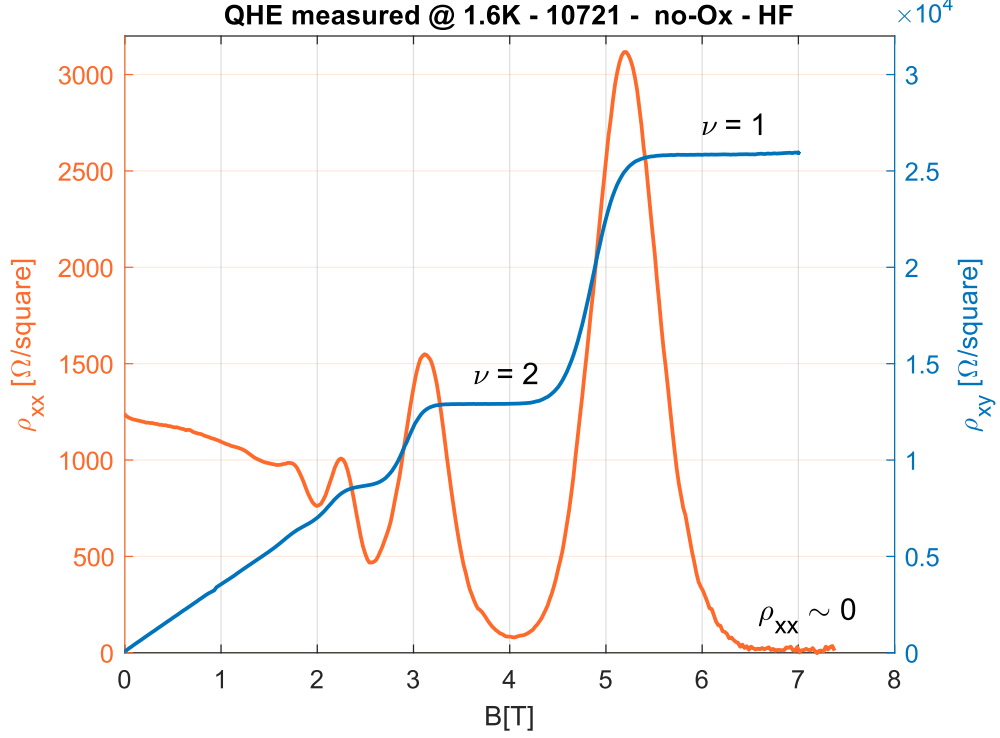
Figure 13: ρ_{xx} and ρ_{xy} plotted as a function of the applied magnetic field, sweeping from 0 to 7.5T at 1.6 K.

Two plateaus in ρ_{xy} are well evident, corresponding to a filling factor ν of 1 and 2. Another interesting behaviour is in the two longitudinal resistivity minimums, where $\rho_{xx} \sim 0$: in this situation electrical conduction takes place only in the edge states. Unfortunately the measurement carried on the uncleaned device provided a disturbed result, without a clear physical interpretation.

10721 oxide-no-gate The following device to be measured is a 10721 Hall bar with oxide on top. The same analysis explained before was performed, and it resulted in a mobility $\mu = 5.88 \times 10^4 \, \text{cm}^2/\text{Vs}$ and a carrier density $p = 9.4 \times 10^{11} \, \text{cm}^{-2}$. These values are quite relevant, because of the relatively high values of mobility and density, compared with devices without the oxide

on top. This result can be explained considering that the oxide includes a
high number of negative charges, replacing the role of the bias voltage in
populating the quantum well. This hypothesis is supported by the fact that
it is known in literature that amorphous Al_2O_3 layers grown using different
deposition techniques contain a significant density of negative charges of still
unclear origin [55].

QHE on 10721 oxide-no-gate   In Figure 14 we show the quantum Hall effect
measurement carried on this sample.
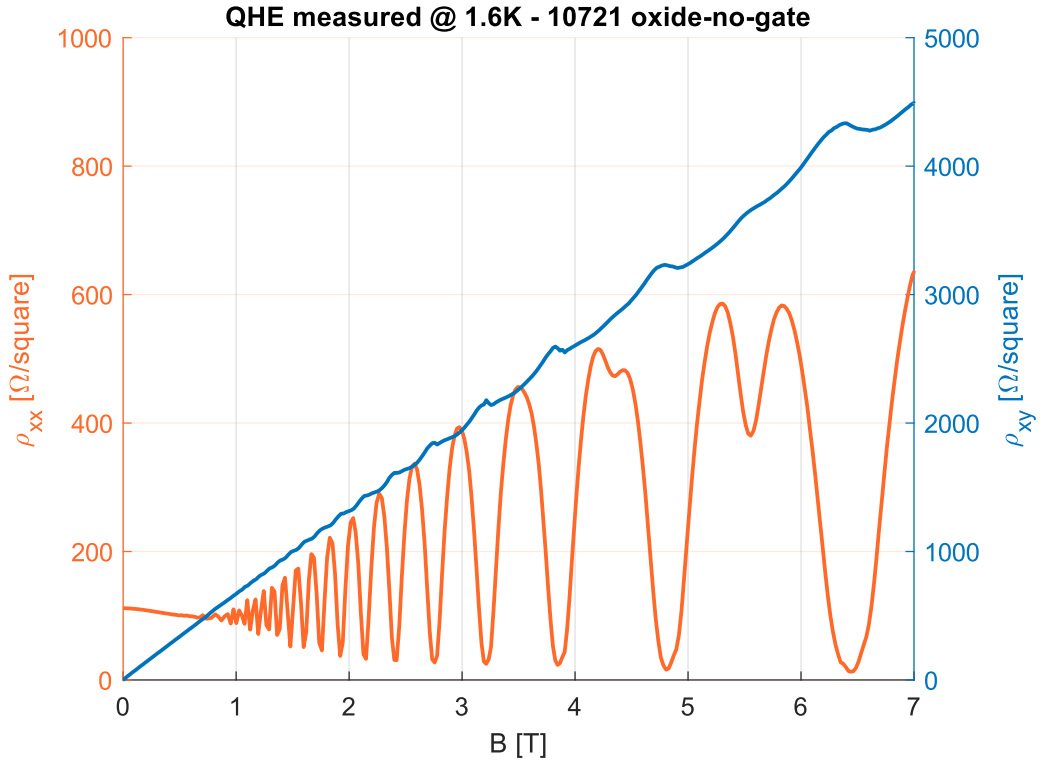
Figure 14: ρ_{xx} and ρ_{xy} plotted in function of the applied magnetic field, sweeping from
0 to 7 T at 1.6 K. Spin-splitting is present above 4 T, and the ρ_{xy} behaviour is anoma-
lous, failing to show clear quantum Hall effect plateaus.

Once again, ρ_{xx} is near to zero in correspondence of the the high-field min-
imums, but in this plot the most interesting feature is the anomalous be-
haviour of ρ_{xy}, associated with a different shape of ρ_{xx} peaks respect to the
previous results. This behaviour can be reproduced exploiting a numeri-
cal simulation in which the Fermi energy oscillates when the magnetic field
increases (and Landau levels appear and grows in amplitude), in order to

respect the charge conservation principle. On the contrary, the standard behaviour predicted for the quantum Hall effect is well explained by a model in which the Fermi energy is kept fixed to its original value by the presence of localized states, and the levels cross periodically this value. Further analysis are needed to understand the physics behind this interesting phenomenon.

Shubnikov–de Haas oscillations analysis on 10721 oxide-no-gate   From Shubnikov–de Haas oscillations it is possible to extract important parameters, such as the effective mass and the Dingle ratio. Furthermore, the periodicity of the oscillation is inversely proportional to the carrier sheet density. As explained in section 3, this value is the real sheet density, since approximations were made in the classical Hall effect theory, but at low temperature the two values are expected to be similar. From this analysis the value $n_{SdH} = 9.43 \times 10^{11} \, \text{cm}^{-2}$ is obtained. The strong agreement between the Hall density and the SdH density indicates that only one 2D carrier gas plays a role in the transport, and so only one sub-band contributes to electrical conduction [8].

In order to extract the α and m^*, SdH oscillations have been measured at 1.6, 2.5, 3.5, 4.5, 5.5, 6.5, and 7.5 K. A peak and its corresponding magnetic field were selected, then the temperature dependence of the relative resistivity value of the peak was studied. First of all, the maxima and the minima were interpolated by two polynomials, and from the average of these two the slowly varying magnetoresistance ρ_{MR} was obtained. In order to isolate the oscillations, the magnetoresistance was subtracted from the experimental data which was then divided by its value.

$$A = \frac{\rho_{xx} - \rho_{MR}}{\rho_{MR}} \tag{4.1.1}$$

In this way the relative amplitudes of the oscillations were found. The choice to divide by the slowly variable magnetoresistance is not unique in literature. In some articles, the amplitudes are divided by ρ_0, corresponding to

the value of ρ_{xx} at zero magnetic field, which is assumed to be constant for all magnetic fields. In this analysis the first approach was chosen, but it was observed that the two methods differed very little. The selected peaks for effective mass extraction are at 2.57 T, a value chosen to avoid the spin splitting events occurring at higher fields, while having a significant amplitude for the peaks. Figure 15a shows that the position of the peak is almost temperature independent, meaning that the 2D carrier density is constant at these different temperatures. The result is an $m^* = 0.12m_e$, a value in good agreement with similar structures in literature [17, 24, 52, 56]. It is relevant to underline that this is the value for the in-plane effective mass and it is practically half that of the heavy hole mass in bulk Ge.

(a)

(b)
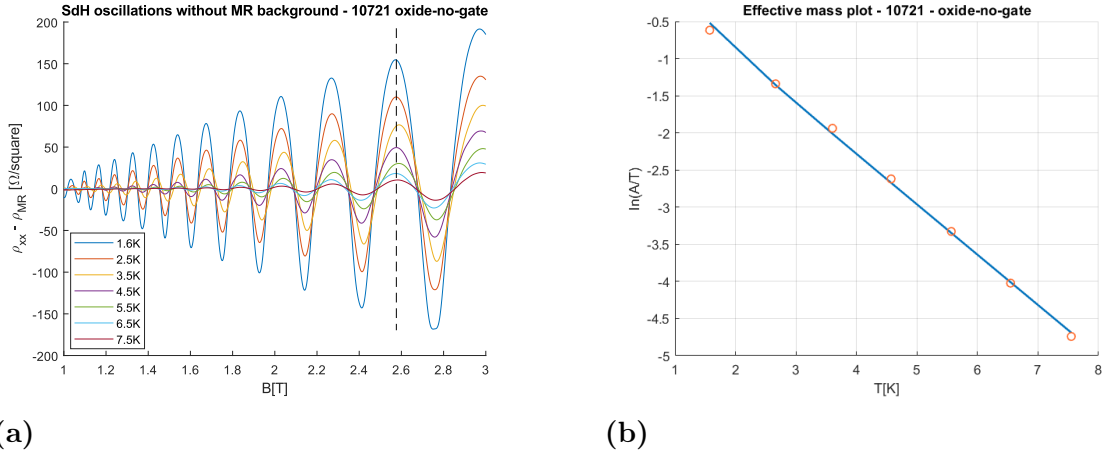
Figure 15: (a) Normalized SdH oscillations of ρ_{xx} with B sweeping from 1 to 3 T for 10721 oxide-no-gate. The dashed line indicates the peaks chosen for the m^* extraction (b) Effective mass plot: $\ln(A/T)$ vs. T.

After the extraction of the in-plane effective mass, it is possible to calculate the Dingle ratio from the Shubnikov–de Haas oscillations envelope at 1.6 K in the range between 1 and 3 T. The value is $\alpha = 3.0$, however, as depicted in Figure 16, the Dingle ratio is clearly not constant with the applied field.
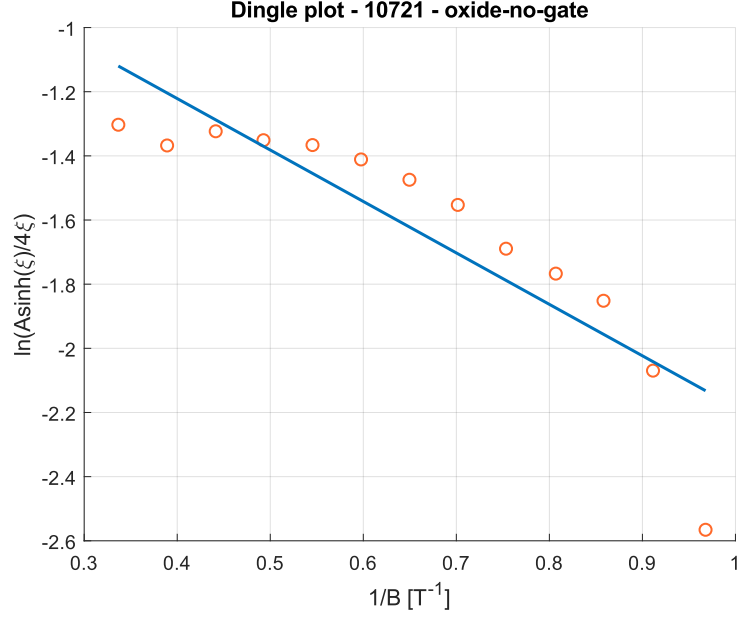
Figure 16: Dingle plot of device 10721 oxide-no-gate, obtained analyzing the curve at 1.6 K.

In a 1991 article [33], Coleridge states that a non-constant behaviour of the Dingle ratio is well justified by inhomogeneities and field dependent dephasing due to a distribution of densities in the 2D carrier gas. This explanation seems to be suited to our situation, in fact the population of the quantum well in this device is not activated by a uniform potential applied by means of a metal gate, but it is caused by the high amount of charges present in the oxide, whose distribution is reasonably assumed to be non uniform. However, an empirical fitting has been performed, hypothesizing a linear dependence of α respect to $1/B$, providing this result, and the plot in Figure 17:

$$\alpha = 4.04 - 4.33\frac{1}{B}$$

Figure 17: Dingle plot of sample 10721 oxide-no-gate. The superimposed fitting has been performed assuming a linear dependence of α respect to $1/B$
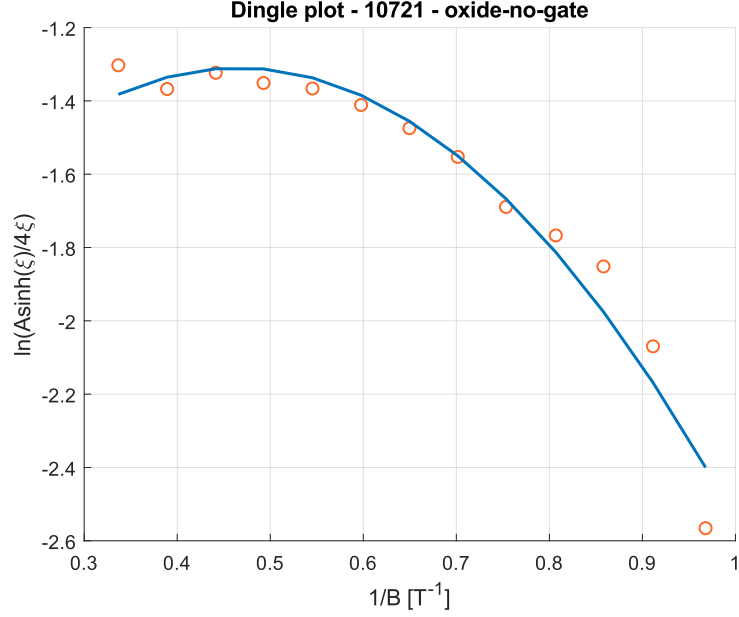
Mobility Spectrum analysis on 10721 oxide-no-gate In order to determine if a low-mobility surface conduction channel is present, ρ_{xx} and ρ_{xy} have been measured at 20 K and 40 K. At cryogenic temperatures the participating carriers should be only those in the Ge channel. When the sample is heated up the SiGe bulk of the device can contribute to the conduction due to background doping, or conduction can be present in a 2DHG formed at the sample surface. This means that now in the device there are two parallel conduction channels. As was explained in section 3 this situation could not be studied with classical Hall effect analysis, since now R_H and ρ_{xx} are no longer constant with a changing magnetic field.

These temperatures are supposed to be high enough to suppress quantum effects, such as the formation of Landau levels. On the contrary this does not mean that at low temperature parallel conduction is always excluded. In some samples analysed in this thesis a slowly varying magnetoresistance was observed, superimposed on the expected Shubnikov–de Haas behaviour at low temperature. This would require us to assume a parallel conduction channel even at cryogenic temperatures. For this reason, the classical magnetoresistence was computed interpolating all the maxima and all the minima

and then it was subtracted in order to isolate the quantum behaviour, as shown in Figure 18.
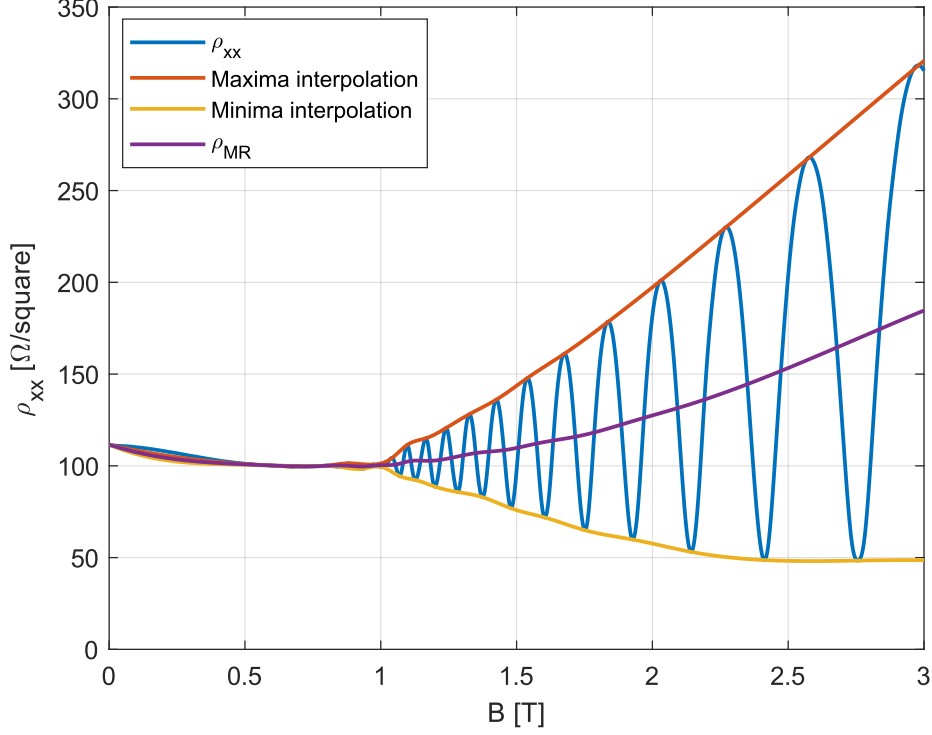
Figure 18: Shubnikov–de Haas oscillations in ρ_{xx} measured at 2.5 K, superimposed on a slowly varying magnetoresistance for 10721 oxide-no-gate

As depicted in Figure 19, the mobility spectrum at 20 K shows a peak relative to a channel with a mobility $\mu = 5.87 \times 10^4 \, \mathrm{cm}^2/\mathrm{Vs}$ in excellent agreement with the extracted Hall mobility ($\mu_H = 5.88 \times 10^4 \, \mathrm{cm}^2/\mathrm{Vs}$), and the absence of low-mobility peaks. The mobility spectrum at 40 K shows the same situation, with mobility values slightly lower, as expected.

Figure 19: Mobility spectrum of the 10721 oxide-no-gate sample. The presence of a single peak at the expected mobility suggests the absence of a parallel channel.

Percolation Density of 10721 In absence of working gated structures, it was impossible to obtain a μ vs n_s data-set need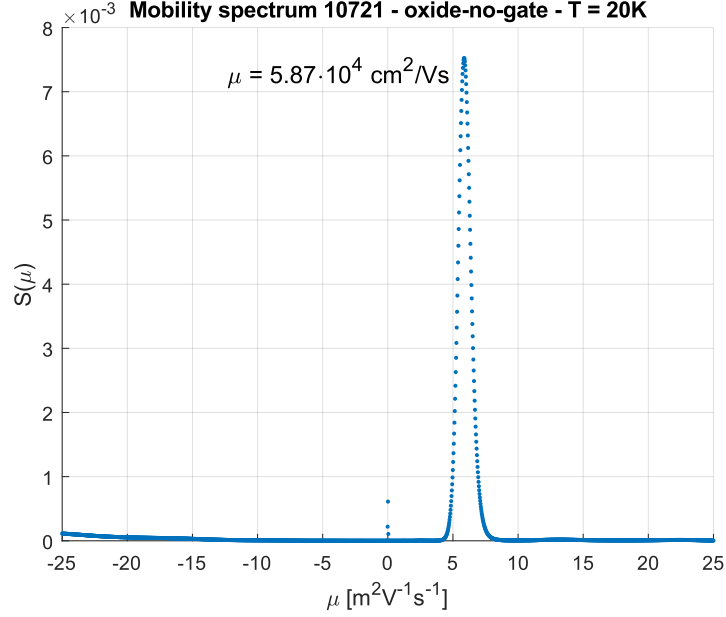ed to extract the percolation density. However, some 10721 gated devices, now broken, were measured by G. Tavani, and featured a $n_p = 4.2 \times 10^{11}$ cm^{-2}. This value is reported in order to be compared with 10820 percolation density extracted in a next section.

A reliable percolation density extraction requires stable measurements in a voltage range close to the device threshold. Some fabrication issues on 10822 and 10818 prevented us from obtaining this condition, so their percolation density has not been extracted. This issues have been solved with a new Hall bars design, as later explained. When comparing n_p of 10721 with the value obtained for 10820 it must be taken into account that the first result has been obtained with the old, less satisfactory, design, and it could be shifted towards higher values.

4.1.2 Sample 10822

The 10822 sample has been grown as an exact copy of 10721, with the aim to compare the data, evaluating their consistency, and to perform the analysis

on the gated devices. The 10822 device with deposited Al_2O_3 and no metallic gate showed a Hall mobility $\mu_H = 9.88 \times 10^4 \, cm^2/Vs$ and a Hall density $n_H = 7.54 \times 10^{11} \, cm^{-2}$.

QHE on 10822 oxide-no-gate The quantum Hall effect measurement was similar to that on 10721, with the difference of a superimposed magnetoresistance preventing the zero longitudinal resistivity condition, as depicted in Figure 20:
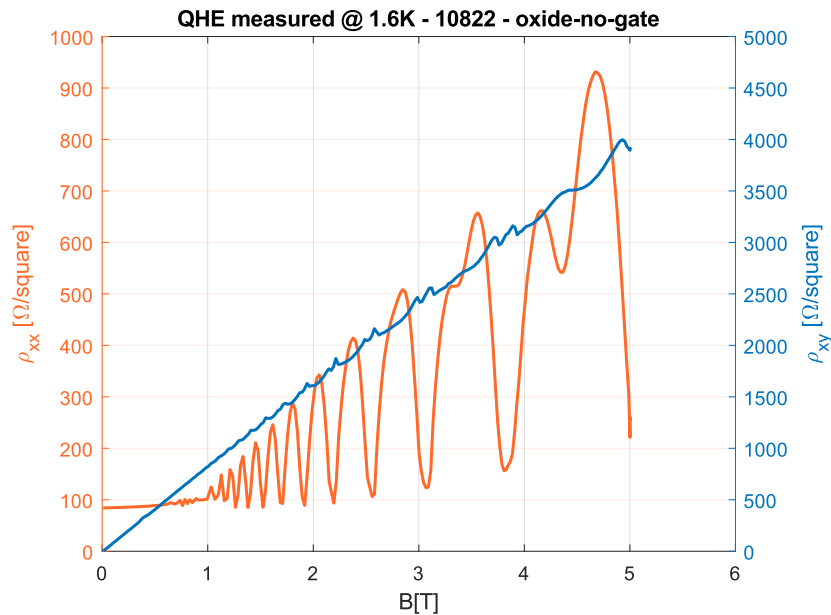
Figure 20: Quantum Hall effect measured on 10822 with oxide but without top metal gate. The magnetic field range is 0–5 T, since that was the operational limit of the cryostat at that time.

SdH oscillations analysis on 10822 oxide-no-gate The density extracted from the Shubnikov–de Haas oscillations is $n_{SdH} = 7.15 \times 10^{11} \, cm^{-2}$, in good agreement with the Hall density.

Mobility Spectrum analysis on 10822 oxide-no-gate The mobility spectrum at 20 K shows a main peak corresponding to a mobility $\mu = 8.26 \times 10^4 \, cm^2/Vs$, and a higher-mobility secondary peak whose interpretation needs further investigations, to understand if it is an error introduced by the algorithm itself,

or if it has a physical explanation. However the mobility spectrum confirmed the absence of a low-mobility superficial parallel channel.
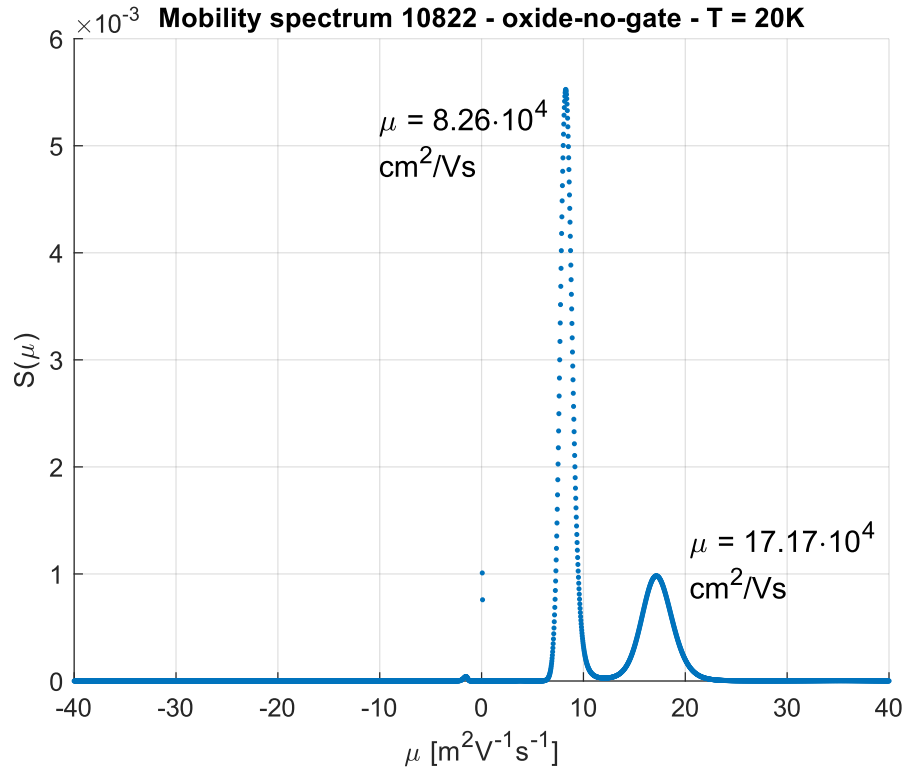
Figure 21: Mobility spectrum of the 10822 at $T = 20$ K. The secondary peak at higher mobility does not have a clear interpretation.

10822 gated devices   For the gated 10822 devices the Hall mobility and Hall density have been calculated for many different gate voltages, with the results in Figure 41a and 41b.

(a)

(b)

Figure 22: (a) Mobility and density plotted as a function of bias voltage at $T = 1.6$ K for 10822. (b) Mobility plotted as a function of 2D density at $T = 1.6$ K for 10822.

Some relevant information can be extracted from these two plots:

- The device turns on at $V_g = -0.2\,V$, meaning that the Schottky contact of the metal gate is enough to compensate and overcome the effect of the charges in the oxide. Thus, a negative potential is needed to populate the channel with a 2DHG.

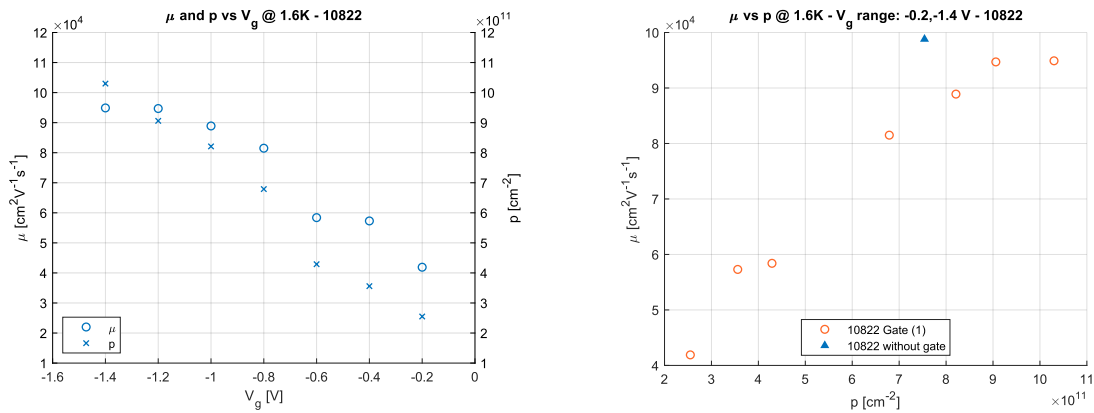- The mobility grows with the absolute value of the bias voltage, then saturates to a value similar to the mobility of the oxide-no-gate device. This behaviour will be even more evident in samples discussed later, suggesting that the charges brought by the oxide are able to saturate the conduction channel.

QHE on 10822 gated device   Shubnikov–de Haas and quantum Hall effect measurements have been carried on the 10822 sample, but the device was affected by a serious current leakage through the top gate, which limited the maximum bias voltage which could be applied.

Another problem was that measured values for ρ_{xx} and ρ_{xy} were extremely disturbed and often not physically realistic, e.g. the presence of zones at negative resistivity, as one can see in Figure 23:
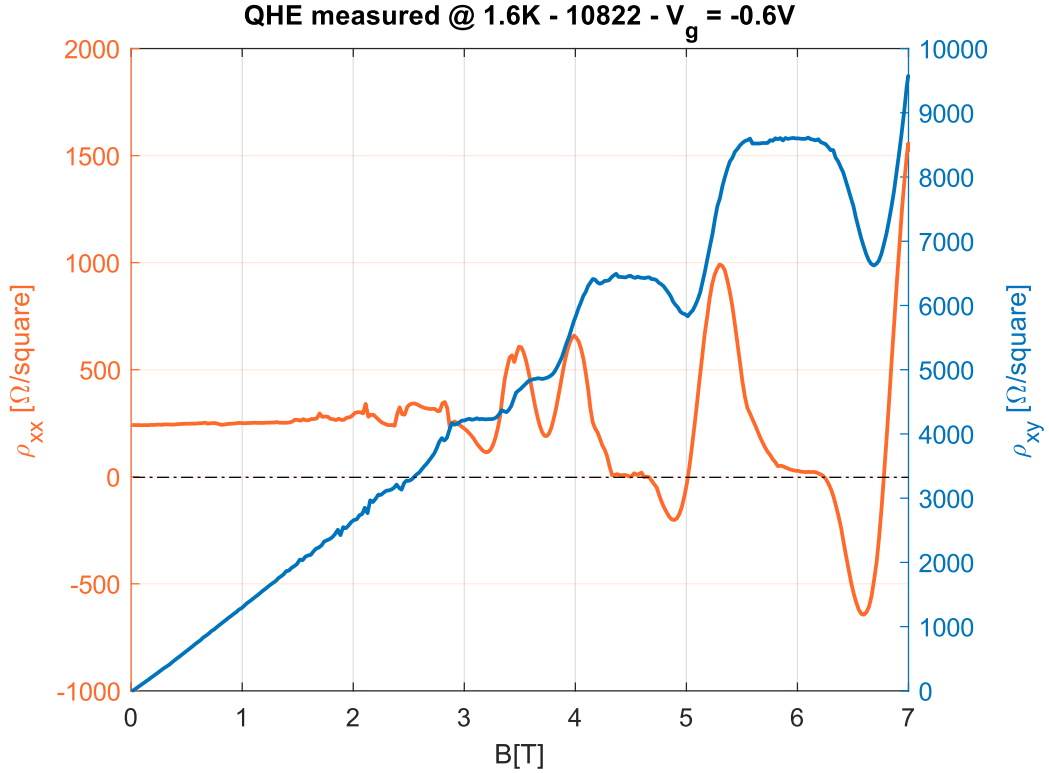
Figure 23: Quantum Hall effect measured on 10822 sample. The measurement is evidently disturbed, and ρ_{xx} goes negative, which is a result clearly not compatible with the physics of the structure.

These issues were mitigated if the gate voltage was increased towards more negative values, or increasing the current injected into the Hall bar, to the cost of heating up the 2DHG. This behaviour suggested that they are not related to the leakage through the oxide (otherwise their influence would have been proportional to the absolute value of the bias voltage). One possible explanation is that, at low bias, the very thin voltage probes on the Hall are turned off, so that they can not conduct properly, distorting the measured signal.

In order to overcome this problem, it has been decided, in accordance with IST, to change the design of the future Hall bars. In the new *body gate* design, the metal for the top gate is not deposited on the probes, exploiting the fact that the oxide brings the conductivity of the sample to its maximum value. This strategy is also expected to mitigate leakage phenomena arising from the proximity between the metallic gate and the metallic eletrical con-

tact pads.

SdH oscillation analysis on 10822 gated device Two identical devices were fabricated on 10822, and they both have been measured, but the second device gave results very similar respect to that discussed above, and it also featured the same issues and problems. However, on the second device, at high bias, it has been possible to measure a few oscillations, sufficiently stable to estimate the effective mass and the Dingle ratio:

	$V_g = -0.9V$	$V_g = -1.1V$
$\mu\,[\;\mathrm{cm}^2/\mathrm{Vs}\;]$	8.92×10^4	9.30×10^4
$p\,[\;\mathrm{cm}^{-2}\;]$	7.49×10^{11}	8×10^{11}
$m^*\,[\;\mathrm{kg}\;]$	$0.11 m_e$	$0.11 m_e$
α	8.45	6.73

**Table 2:** n_H, μ_H, m^*, and α extracted at two different values of bias voltage V_b.

The value of the Dingle ratio $\alpha \gg 1$ suggests that small-angle scattering mechanisms, e.g. remote impurity scattering, are dominant.

τ_q values can be easily calculated, and they correspond to 0.66 and 0.86 ps. Knowing this, it is possible to calculate the broadening Γ of a Landau level as

$$\Gamma \sim \frac{\hbar}{2\tau_q} = 0.49\,\mathrm{meV} \;\; \mathrm{and} \;\; 0.38\,\mathrm{meV}$$

It is relevant to underline that, as one can see in Figure 24a and 24b, the assumption of constant Dingle ratio is more reasonable, with respect to 10721. As already discussed, this can be due to the fact that an applied bias through a metallic gate is a much more uniform potential than that generated by charges trapped in the Al_2O_3 layer.
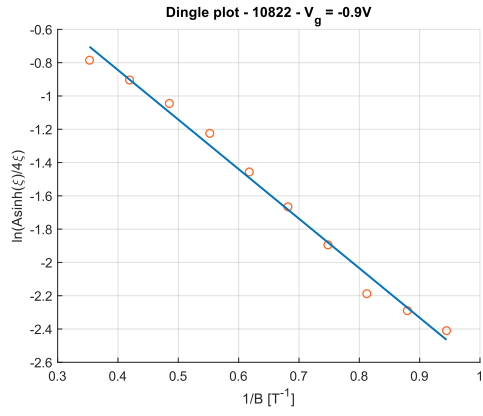
(a)
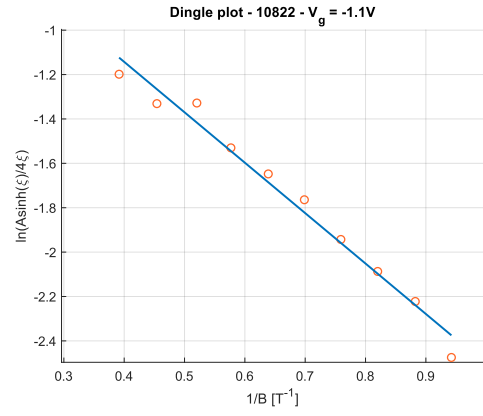
(b)

Figure 24: Dingle plot for 10822 at (a) V_g = -0.9 V (b) V_g = -1.1 V. Even if some outliers are present, the linear fitting is much more consistent than in 10721.

4.2 MBE Samples

4.2.1 Sample 10818

Sample 10818 is a structure whose graded buffer layer was grown at L-NESS via LEPECVD, while the Germanium QW stack has been grown by MBE in Beijing by the group of Jianjun Zhang at the Chinese Academy of Sciences.

Before discussing electrical measurements, it is important to underline that an XRD analysis, performed after the MBE growth, shows that the barrier of the 13 nm thick Ge QW has a Ge content of 62.6%, compared to the nominal 70% Ge content of the buffer layer.
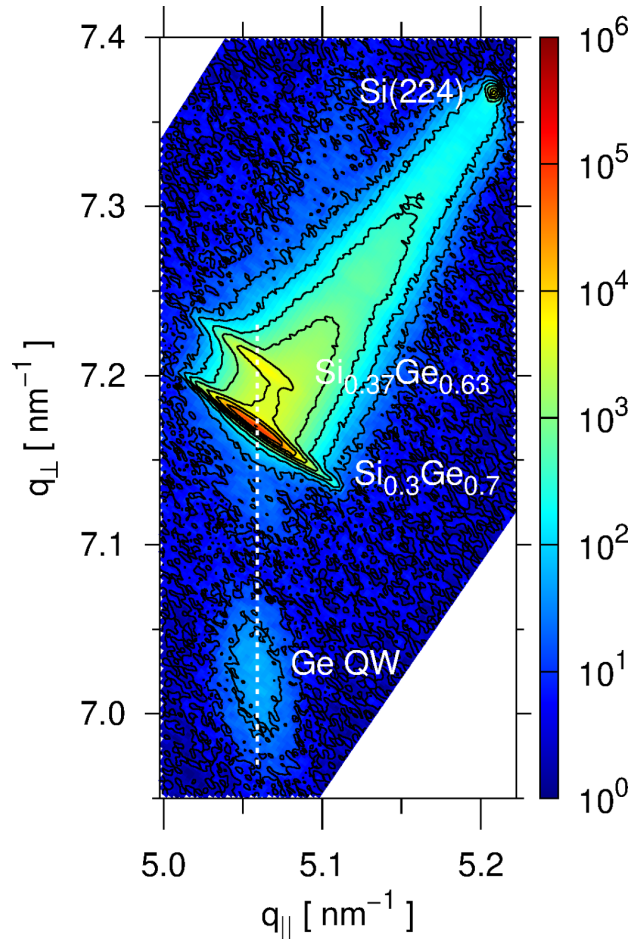

Figure 25: XRD analysis performed by D. Chrastina at the L-NESS. A mismatch between the Ge content of the MBE grown barrier and the buffer layer content is well highlighted.

Another consideration to be taken into account is that 10818 devices were fabricated before the decision to change the Hall bar design, so they are af-

fected by the same problems identified on 10721 and 10822, especially at low bias.

The best low-temperature 2DHG mobility for a Ge/SiGe heterostructure grown by MBE in the literature is 5.5×10^4 cm^2/Vs [57, 58, 59], a value clearly exceeded by LEPECVD (as well as CVD) heterostructures, as demonstrated in the previous section.

10818 oxide-no-gate The first relevant result is the absence of conduction at cryogenic temperatures of a device without the oxide and gate layers: this would suggest that the p-type background introduced with the LEPECVD growth is no longer present in these MBE grown samples.

The Hall measurements performed on a device following oxide deposition, but without top gate, resulted in a mobility value $\mu_H = 3.30 \times 10^4$ cm^2/Vs, with a carrier density $n_H = 1.09 \times 10^{12}$ cm^2/Vs. The relevant role of the deposited oxide in activating the conduction by populating the quantum well can be stressed once again.

SdH oscillation analysis on 10818 oxide-no-gate The Shubnikov–de Haas oscillation analysis confirmed the accuracy of the Hall density value, since $n_{SdH} = 1.07 \times 10^{12}$ cm^2/Vs.
Shubnikov–de Haas oscillations have been measured for six different temperatures, sweeping from 1.6 to 5 K in order to extract m^* and α.
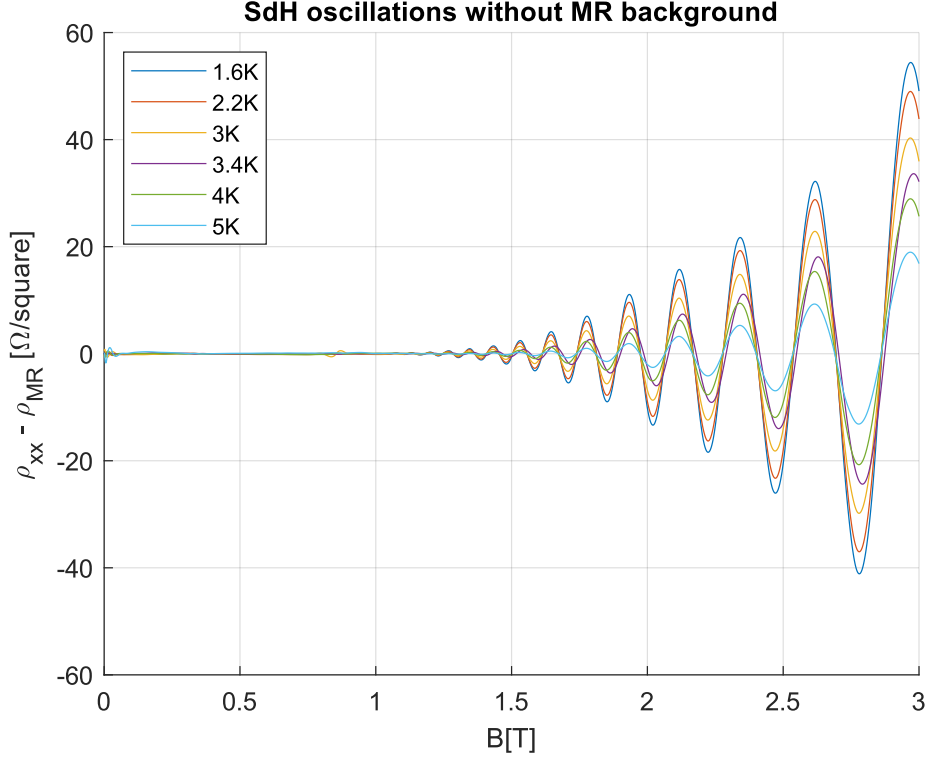
Figure 26: Shubnikov–de Haas oscillations of ρ_{xx} measured at different values of temperatures. The background of a slowly varying magnetoresistance has been subtracted.

(a)

(b)
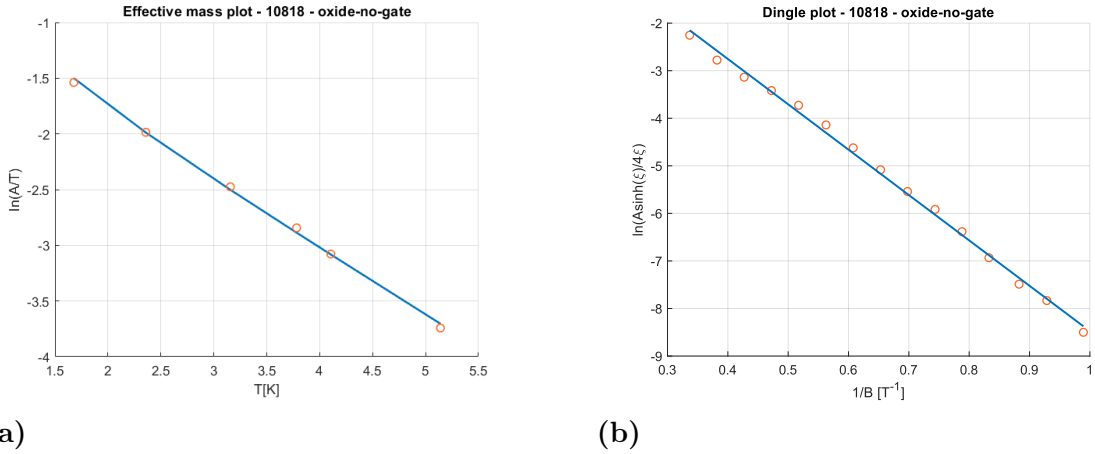
Figure 27: (a) $\ln(A/T)$ plotted as a function of T in order to extract the in-plane effective mass of the carriers for 10818. (b) Dingle plot for 10818 sample without top metal gate. In this case the assumption of considering α as constant respect to B seems well justified.

The values obtained are $m^* = 0.117m_e$ and $\alpha = 9.85$. A Dingle ratio $>> 1$ suggests, as stated before, that small-angle scattering mechanisms are dominant. In this particular situation the Dingle ratio is constant with the magnetic field, even if the potential is applied by means of oxide trapped

charges: this matter will require a further investigation, to understand if results change for every device, as the oxide layers are always different, or if the theory predicting a constant α needs to be improved to take into account a field dependence under some circumstances.

τ_q can be easily calculated, and it corresponds to 0.22 ps. Knowing this it is possible to calculate the broadening Γ of a Landau level as

$$\Gamma \sim \frac{\hbar}{2\tau_q} = 1.5\,meV$$

10818 gated device The 10818 device with the metal gate on top was measured to determine μ_H and n_H at different gate voltages:
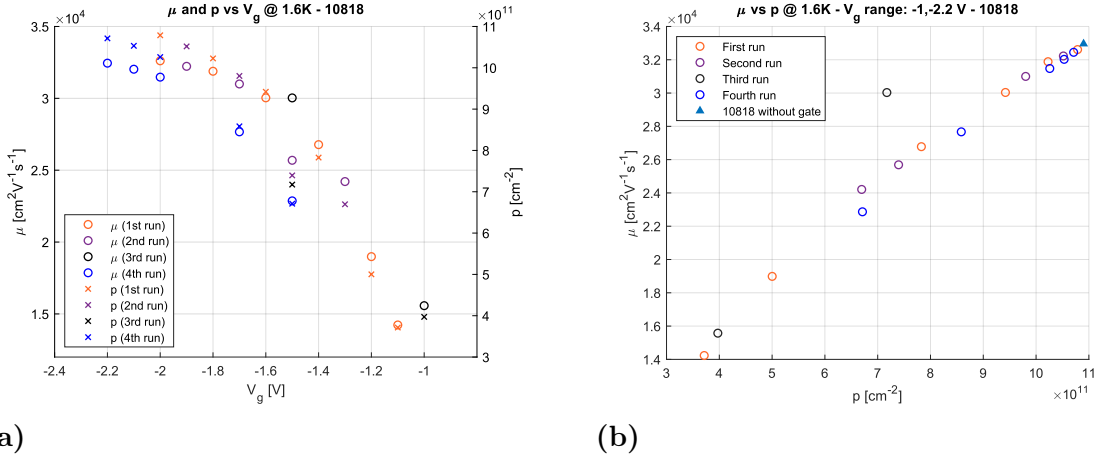

(a)

(b)

Figure 28: (a) Hall mobility and density plotted as a function of the gate voltage. The threshold to turn on the device is significantly higher than V_{th} for 10822. Some different runs have been performed and there is a clear shift of the curve towards more negative bias values. (b) Hall mobility plotted in function of density. The value of the oxide-no-gate device is clearly the upper limit for mobility.

From Figure 28a and 28b, two relevant pieces of information can be extracted:

- The threshold voltage is significantly higher (in absolute value) than that for 10822, meaning that the effect of the work function of the metallic gate is even more effective in de-populating the QW.

- Different runs show that there is a relevant hysteresis effect, with a shift of the μ, p vs V_g curve towards more negative values. This is an issue that must be taken into account when qubits are realized, since the applica-

tion of a confining voltage can shift electrical properties of the material, seriously affecting the measurements' stability and reproducibility.

QHE on 10818 gated device An attempt to measure the quantum Hall effect has been carried out, but unfortunately the magnetic field limit at that time was lowered to 5 T, due to technical problems, and above 4 T the measurements featured jumps and disturbances.
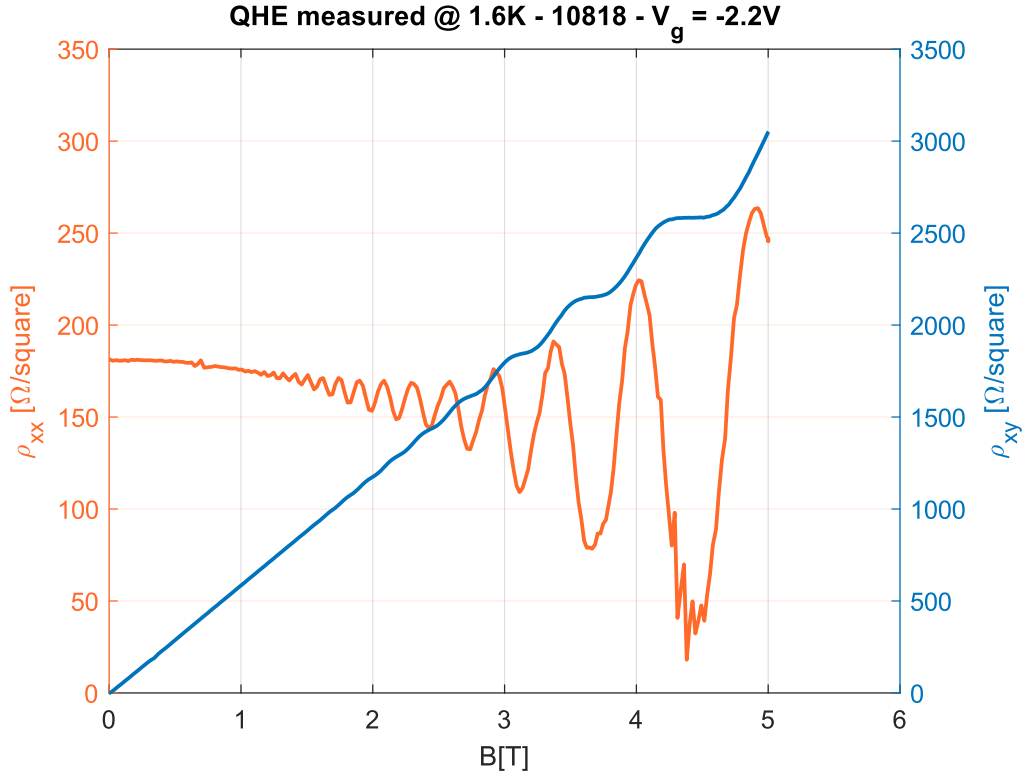
Figure 29: ρ_{xx} and ρ_{xy} measured at 1.6 K, sweeping the magnetic field from 0 to 5 T, at V_g. Shubnikov–de Haas oscillations are clearly present, and ρ_{xy} plateaus can be identified.

SdH oscillations analysis on 10818 gated device However, Shubnikov–de Haas oscillations were stable enough to perform the usual analysis at a gate voltage $V_g = -2.2$ V: $n_{SdH} = 1.06 \times 10^{12}$ cm^{-2}, $m^* = 0.12m_e$, $\alpha = 9.075$.
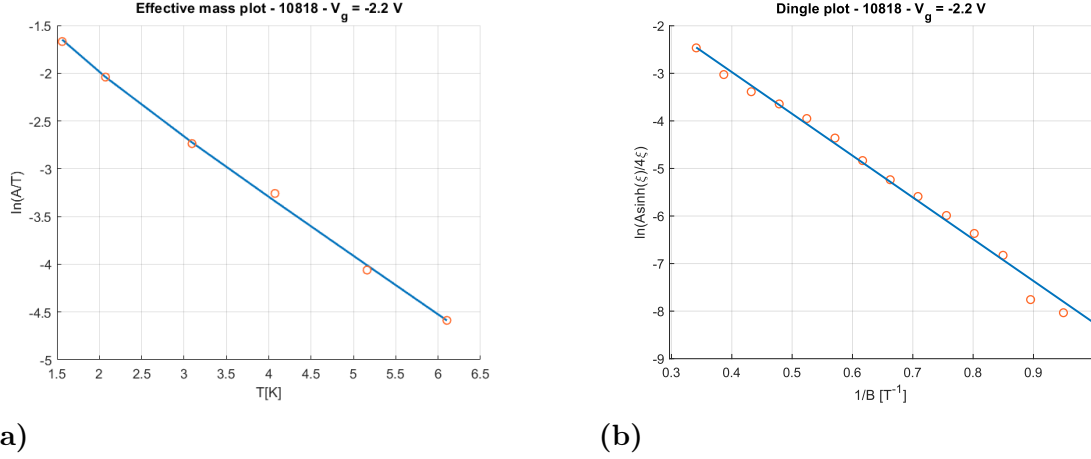
Figure 30: (a) $\ln(A/T)$ plotted as a function of T in order to extract the in-plane effective mass of the carriers. (b) Dingle plot for 10818 with a top metal gate at $V_g = -2.2$ V.

The same considerations made for the oxide-no-gate sample are valid for these data. It is interesting to observe that for 10818 there is no qualitative difference between Dingle plots of the oxide-no-gate and the gated sample, suggesting, as already discussed before, that the dependence of α on the magnetic field should be carefully investigated.

Mobility Spectrum analysis on 10818 gated device   The mobility spectrum analysis confirmed the absence of a low-mobility surface channel.

4.2.2 Sample 10820

The sample 10820 was meant to be an exact copy of the 10818, except for the fact that the germanium quantum well has been grown with isotopically purified ^{72}Ge. This choice should positively affect the performance of the qubits, but in principle it should not affect electrical characterization measurements.

In reality, the 10820 is not exactly the same as 10818, since the Ge content of the SiGe barrier growth by MBE corresponds to the nominal 70%, as the XRD measurement shown in Figure 31 demonstrates.
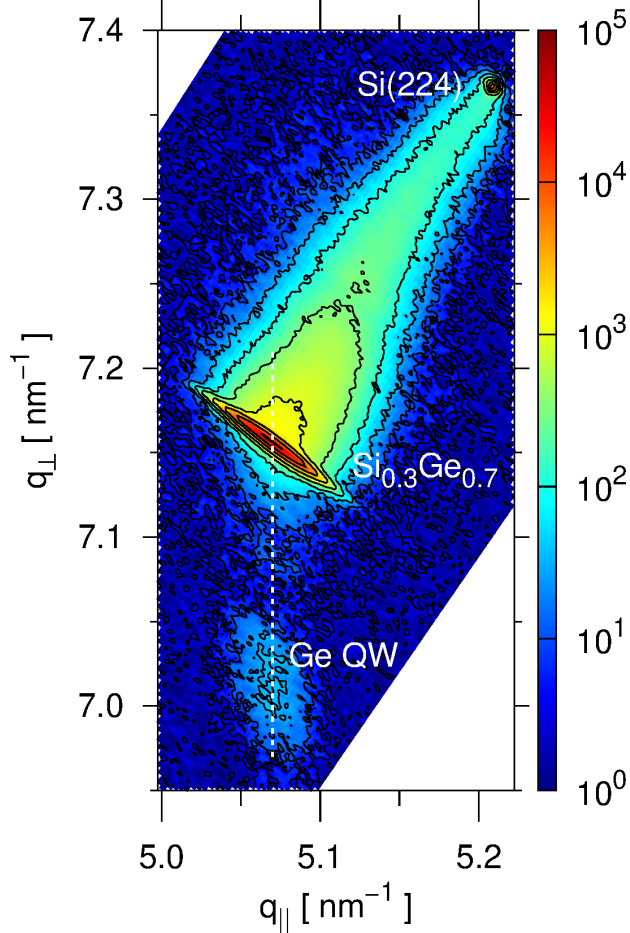
Figure 31: XRD analysis performed by D. Chrastina at the L-NESS. No mismatch between the Ge content of the MBE grown barrier and the buffer layer is detected.

Three different gated devices fabricated on 10820 have been characterized: the first was fabricated following the old design, with voltage probes covered by the top gate; the second and the third devices have been fabricated with the new *body gate* design.

10820 oxide-no-gate   The first measured device was the oxide-no-gate structure: Hall measurements gave $\mu_H = 3.67 \times 10^4 \, \text{cm}^2/\text{Vs}$ and $n_H = 8.23 \times 10^{11} \, \text{cm}^{-2}$; the accuracy of these values has been confirmed by the subsequent extraction of $n_{SdH} = 7.94 \times 10^{11} \, \text{cm}^{-2}$.

SdH Oscillation analysis on 10820 oxide-no-gate In order to extract the effective mass and the Dingle ratio, Shubnikov–de Haas oscillations have been measured at six different temperatures, in a range between 1.6 and 6.5 K (Figure 32).
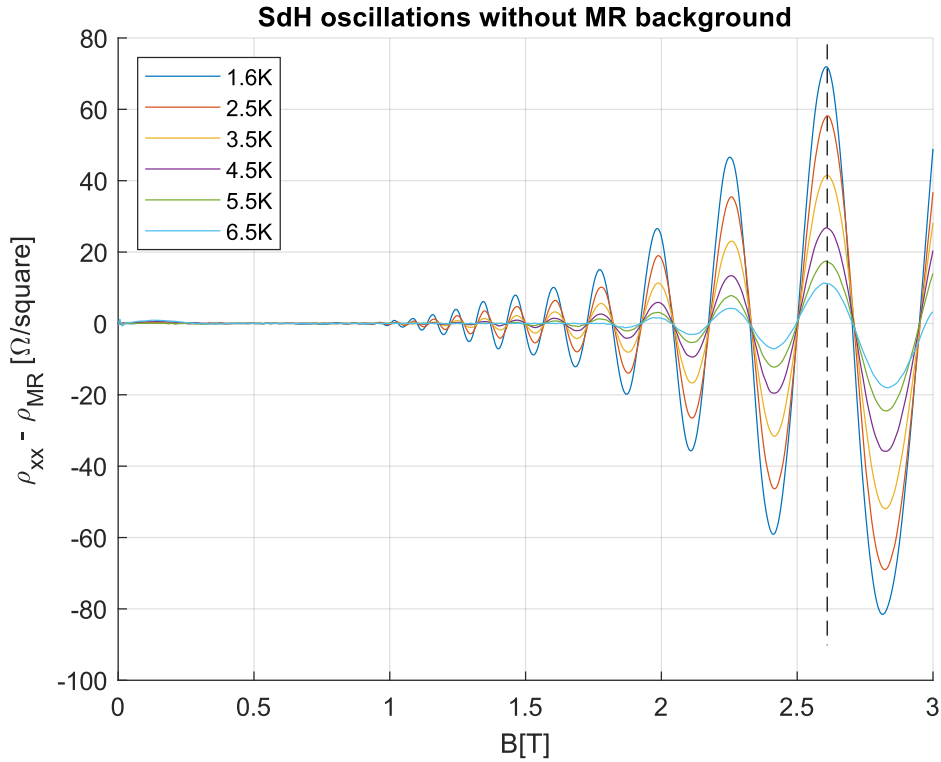

Figure 32: Shubnikov–de Haas oscillations measured on 10820 oxide-no-gate. The dashed line indicates the peaks chosen for the effective mass extraction.
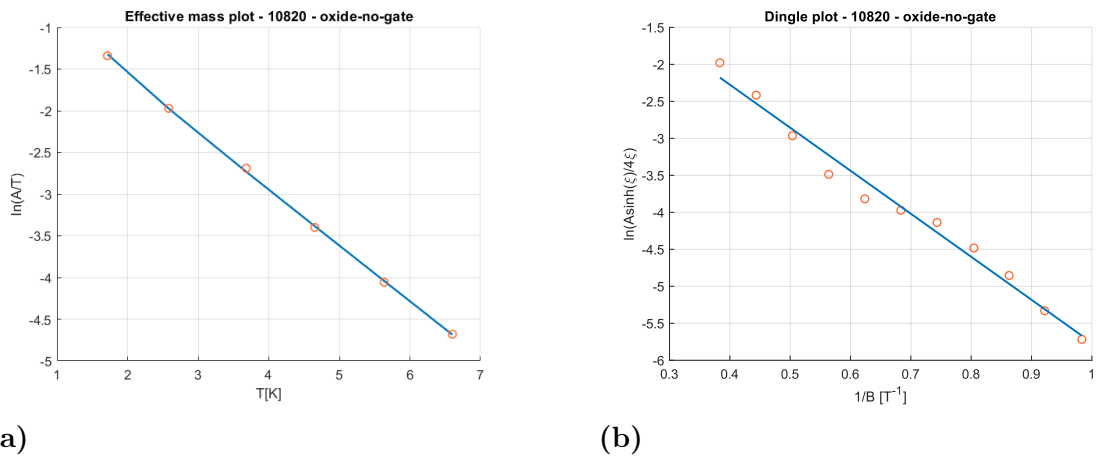

(a)

(b)

Figure 33: (a) $\ln(A/T)$ plotted as a function of T in order to extract the in-plane effective mass of the carriers for 10820 oxide-no-gate. (b) Dingle plot for 10820 without top metal gate for 10820 oxide-no-gate

In Figure 33b it can be seen that the points of the Dingle plot slightly oscillate around the fitted linear behaviour. The extracted $m^* = 0.118 m_e$, while the Dingle ratio $\alpha = 17.22$. This value is almost twice that found for 10818, but it has been confirmed also by the characterization of gated devices, as we will discuss later.

For this value of α, the quantum lifetime $\tau_q = 0.14 ps$, leading to a broadening of the Landau levels $\Gamma = 2.3 \, \text{meV}$.

QHE on 10820 oxide-no-gate A measurement of the Quantum Hall effect has been performed.
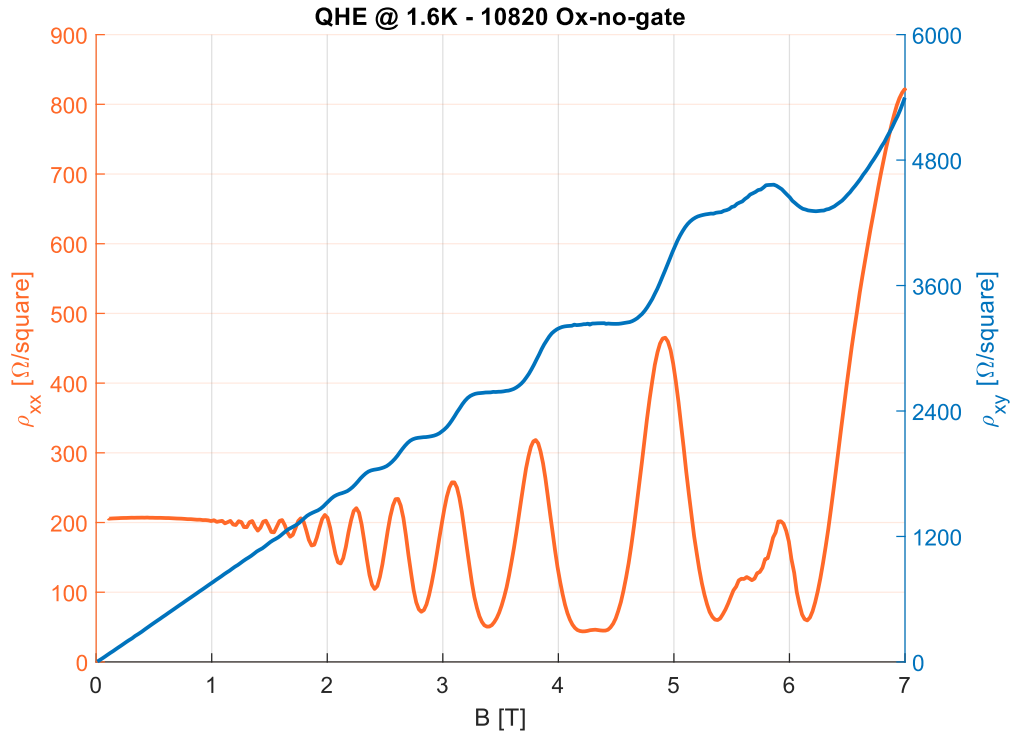

Figure 34: ρ_{xx} and ρ_{xy} measured at T = 1.6 K for 10820 oxide-no-gate. The magnetic field sweeps in a range between 0 and 7 T.

The result is a typical QHE behaviour. In Figure 34 transverse resistivity plateaus are visible and, in the same field ranges, the longitudinal resistivity reaches small values (but never zero). The only unexpected feature is visible

at ~ 6 T.

Mobility Spectrum analysis on 10820 oxide-no-gate   Finally, a mobility spectrum analysis has been carried on the device, at 20 and 40 K. Figure 35 shows the results of the 20 K analysis:
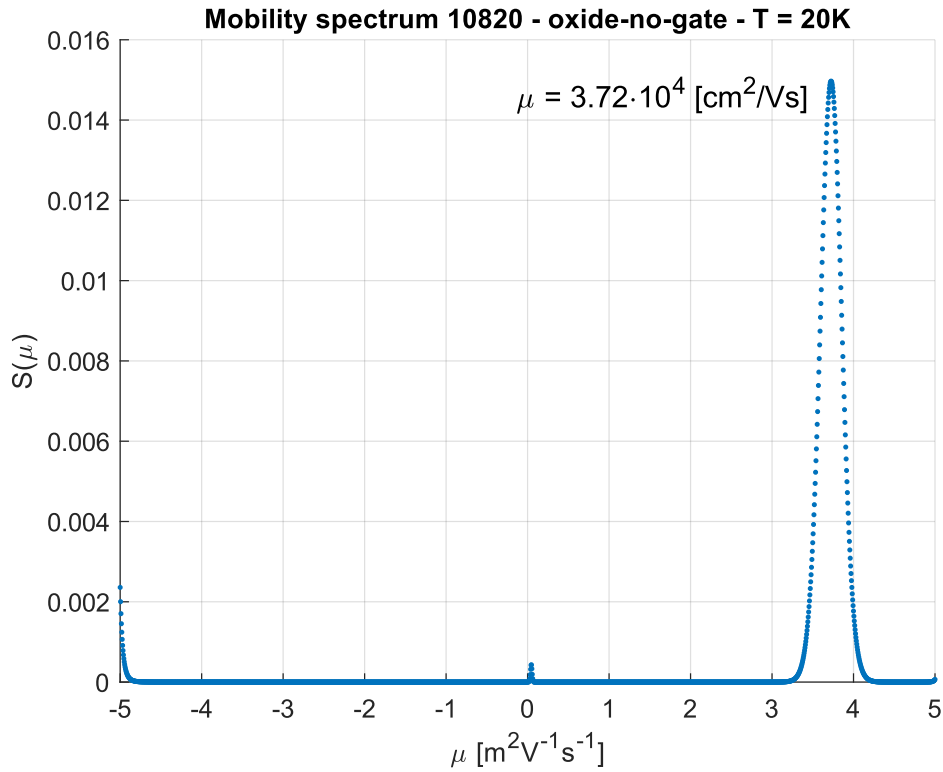
Figure 35: Mobility spectrum of 10820 oxide-no-gate.

A main peak at $3.72 \times 10^4 \, \mathrm{cm}^2/\mathrm{Vs}$ is present; this value is slightly higher than the Hall mobility, and the software compensates it introducing a few non-zero points around $\mu = 0$ and $\mu < -5 \times 10^4 \, \mathrm{cm}^2/\mathrm{Vs}$, without any physical meaning.

10820 gated device - Old design   Unfortunately, the gated device fabricated with the old design was not properly useful, because of an extremely high leakage current, increasing with the bias voltage (Figure 36).
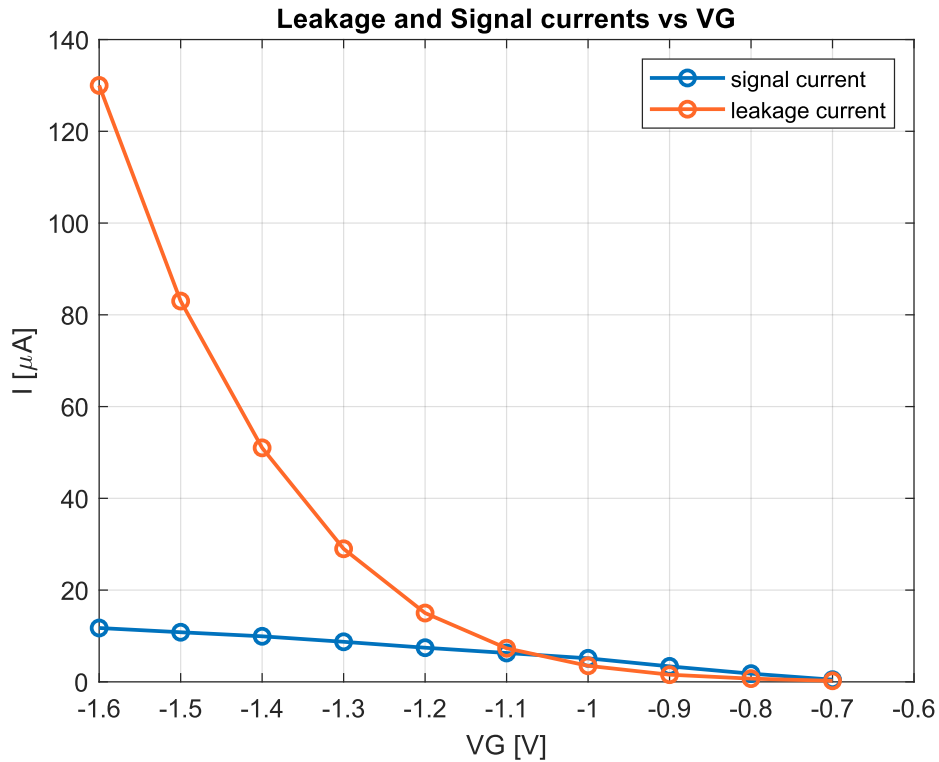
Figure 36: Signal current and leakage current through the gate for 10820 (old design). The dominant contribution is given by the leakage current, making it difficult to make reliable measurements.

Hall mobilities and Hall densities as a function of the voltage bias has been measured, but with unstable results, such that their interpretation is difficult and not particularly interesting, if compared with the results coming later.

10820 gated device (1)   The first device covered with the "body" gate has shown the Hall mobilities and densities in Figure 37a and 37b.
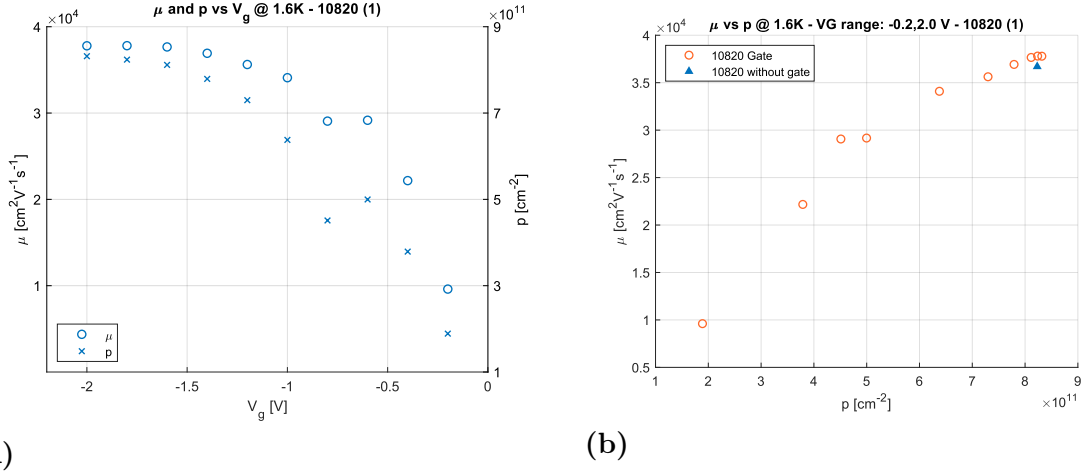
Figure 37: (a) Mobility and density plotted as a function of bias voltage at $T = 1.6$ K. (b) Mobility plotted as a function of 2D density at T = 1.6 K. The triangle represents μ_{ong}, and represents the saturation value for $\mu(n)$.

The threshold voltage is $V_g = -0.2$ V, significantly lower than the threshold value for 10818. Moreover, no leakage has been detected in the range of tens of nA. These two facts suggest that the modification introduced in the fabrication process is useful to obtain more stable and reliable measurements.

QHE on 10820 gated device (1) Quantum Hall effect has been measured at a bias voltage $V_g = -1.8$ V (Figure 38).
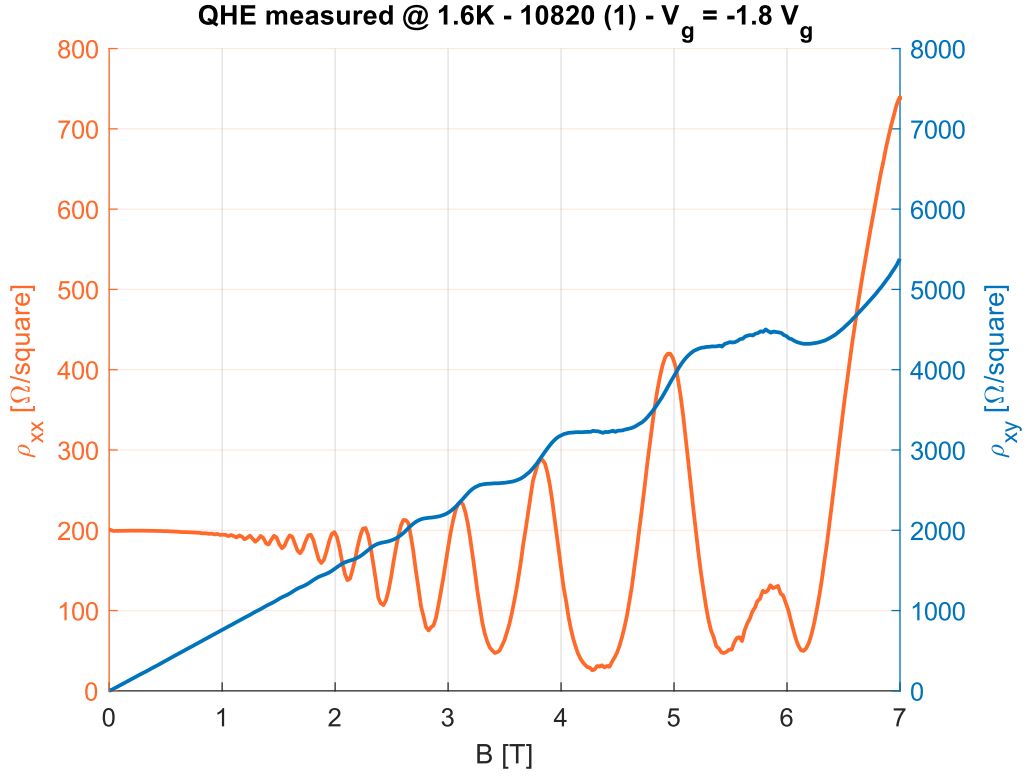
Figure 38: QHE measured at $T = 1.6$ K and $V_g = -1.8$ V for 10820.

The interpretation is similar to that discussed for the oxide-no-gate sample, and the same feature near $B = 6$ T is present.

SdH oscillation analysis on 10820 gated device (1) Shubnikov–de Haas oscillations measured at the same bias voltage allowed us to extract the values for the effective mass $m^* = 0.113 m_e$ and for the Dingle ratio $\alpha = 18.23$. As anticipated, the high value of the Dingle ratio is confirmed for 10820, meaning that the low angle scattering mechanisms are even more dominant than in 10818 despite the similar mobility. Moreover, the behaviour of the Dingle plot is linear, as expected, meaning that α is constant with respect to the applied field (Figure 39). This contributes to increasing the reliability of the value extracted.
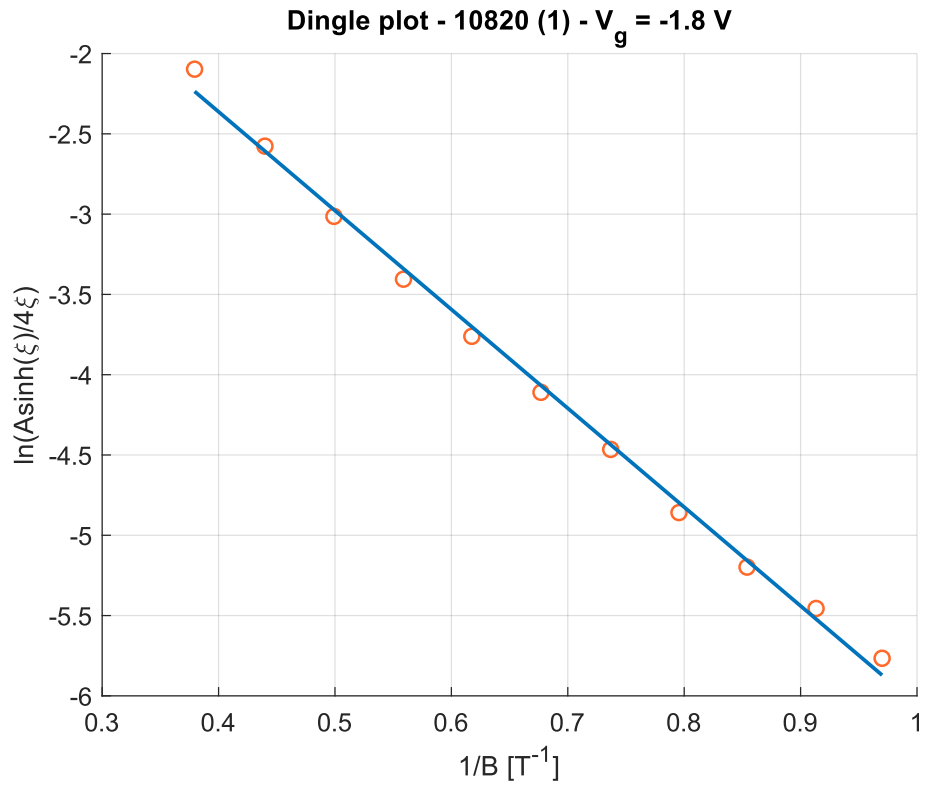
Figure 39: Dingle plot at $V_g = -1.8$ V for 10820 (1)

Mobility Spectrum analysis on 10820 gated device (1) The mobility spectrum analysis has been performed at $V_g = -1.8$ V and the result coincides with the result discussed for the oxide-no-gate sample.
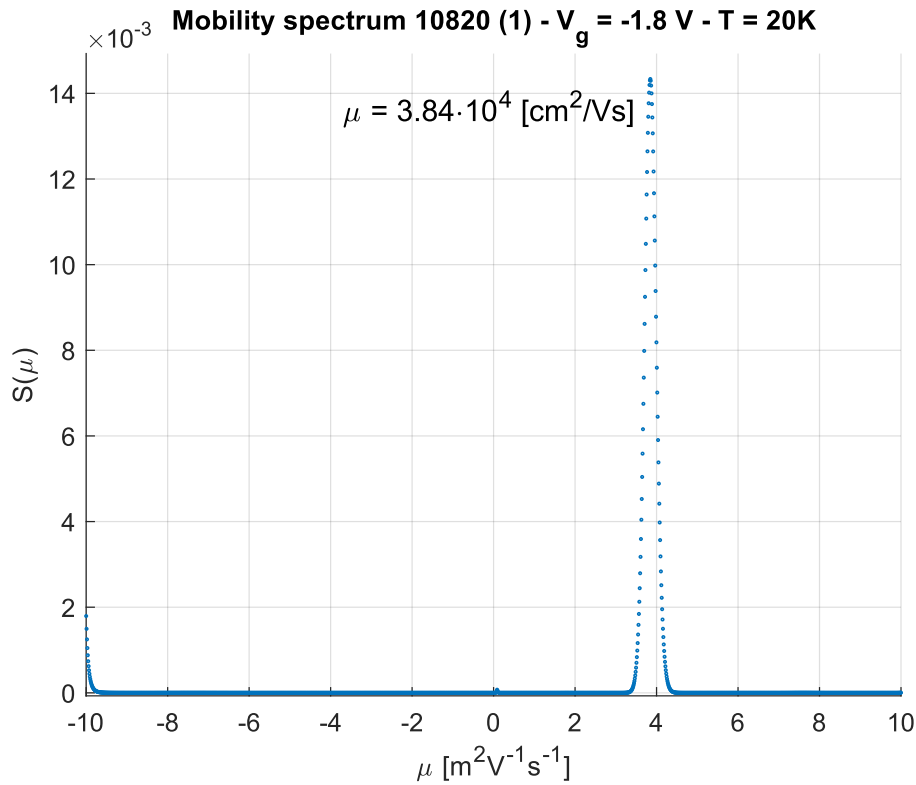
Figure 40: Mobility spectrum of 10820 (1)

10820 gated device (2) The second "body gated" sample turned on even at zero bias, and its extreme stability allowed accurate measurements near the threshold voltage, as depicted in Figure 41a.

(a)

(b)
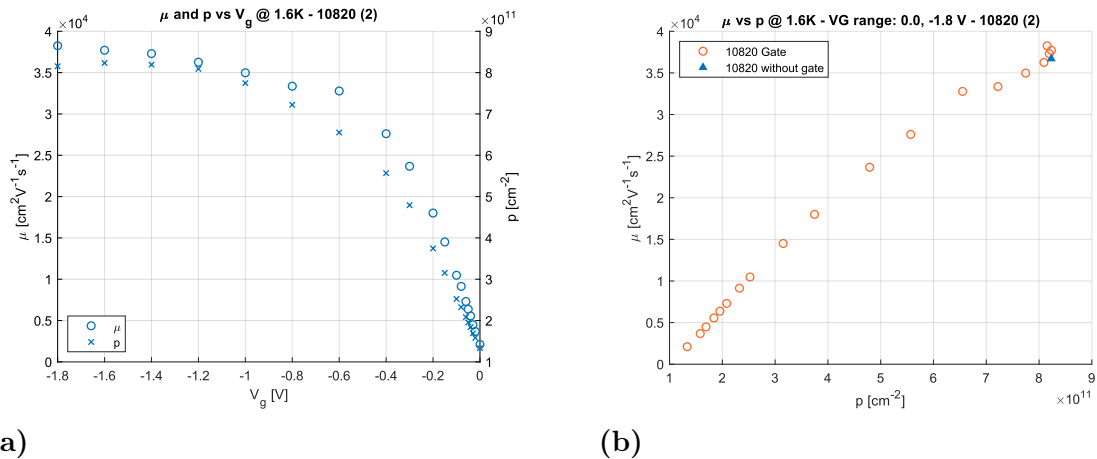
Figure 41: (a) Mobility and density plotted as a function of bias voltage at $T = 1.6$ K for 10820 (2). (b) Mobility plotted as a function of 2D density at $T = 1.6$ K for 10820 (2). The triangle represents μ_{ong}, and represents the saturation value for $\mu(n)$.

QHE on 10820 gated device (2)   This good performance has been exploited, first to measure the quantum Hall Effect at relatively low density (Figure 42) and then to extract the percolation density (Figure 43).
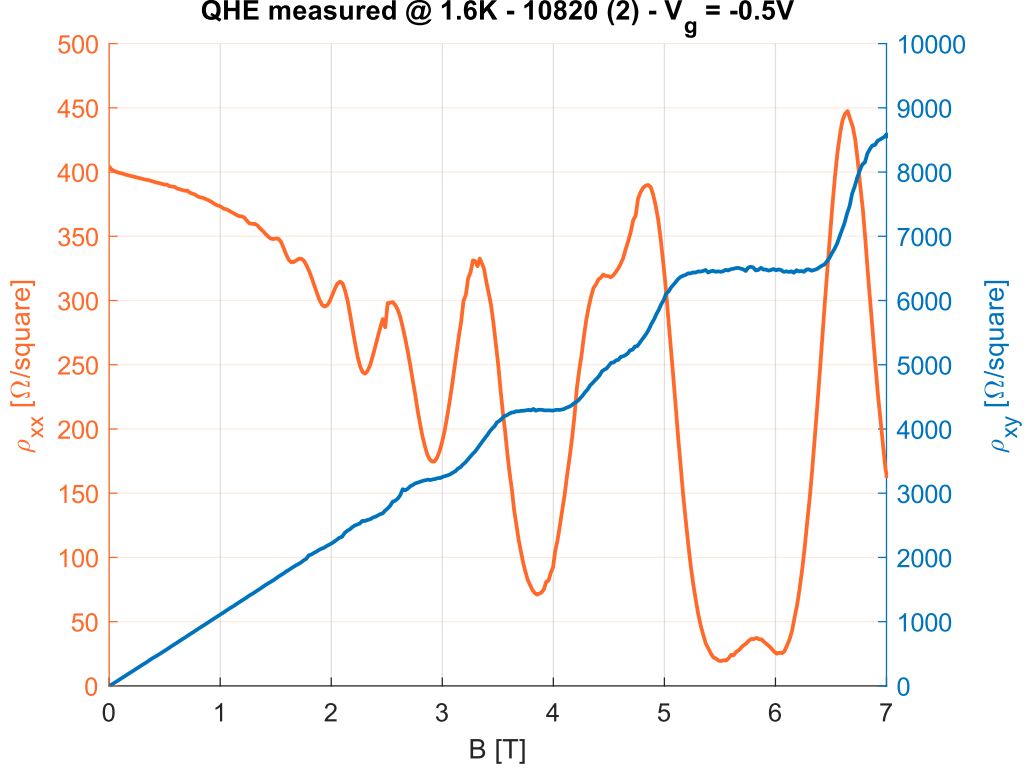
Figure 42: QHE measured at $T = 1.6$ K and $V_g = -0.5$ V for 10820.

The measurement is affected by some noise, but all the typically expected features, such as plateaus in ρ_{xy} corresponding to a $\rho_{xx} \sim 0$, are present, along with a spin splitting effect on the peaks at higher field.

Percolation Density of 10820 gated device (2)   The most important result related to this specific device is that the mentioned stability just above the threshold voltage provides a good data-set to extract the *percolation density*. In order to extrapolate this parameter the conductivity σ is expressed in units of $\frac{e^2}{h}$, then these values are plotted vs. sheet density, and fitted with a function

$$\sigma = A(n - n_p)^p \tag{4.2.1}$$

While A and n_p are used as fitting parameters, the value of the exponent p is critical: as discussed before, it is theoretically fixed at $p = 1.31$, but this value provides a completely unfeasible fitting, as one can see in Figure 43.
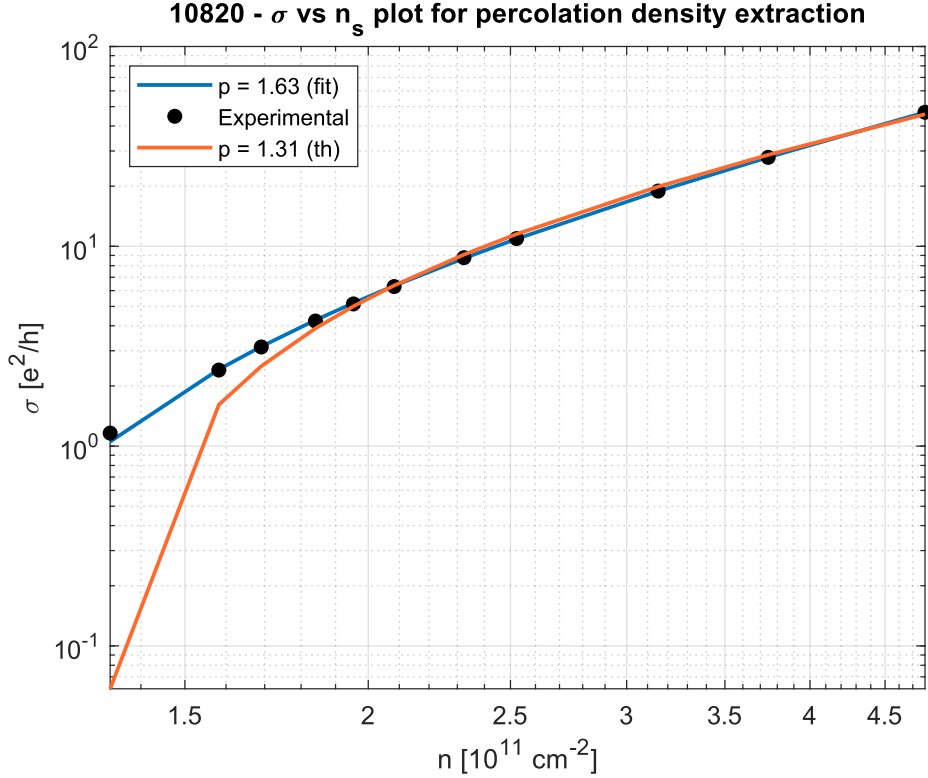
Figure 43: $\sigma(n)$ plot, fitted to extract the percolation density. The blue line is obtained considering p a fitting parameter. The orange line is obtained for $p = 1.31$, and clearly is not suitable to fit the experimental data.

In order to obtain a correct fit, p has been treated as a third fitting parameter: within this approach, $p_{fit} = 1.63$ and the percolation density is $9.6 \times 10^{10} \, \text{cm}^{-2}$.

The value of the exponent is not so dissimilar to the theoretical value, especially if it is taken into account that the measurement has been performed at $T > 1$ K.

Conclusions

This thesis work has the main objective to analyze HMOS structures, in order to study their capability to host quantum dots for quantum computing applications.

The first conclusion about the LEPECVD material is the presence of a p-type background independent from airborne boron contamination. This background doping is not present in the MBE material, where the channel is frozen in absence of Al_2O_3 or bias voltage applied. However the MBE grown Ge features a lower mobility, as expected.

The reduction of oxygen contamination in LEPECVD growth could be a critical step in enhancing 2DHG mobility in the HMOS heterostructure.

The Dingle ratio values extracted are interesting because, despite being higher than 1, they are relatively low, meaning that the quantum lifetime is quite long. It must be taken into account that a high Dingle ratio is not good *per se*: the higher is the Dingle ratio, the longer is τ_{tr} respect to τ_q, but on the other hand, a high mobility already indicates that τ_{tr} is long, and a large α means that τ_q is short.

The next steps regard a deeper investigation of the Dingle ratio values, its dependence on the applied field, and differences between LEPECVD samples and MBE samples, and even between 10818 and 10820 samples, since the isotopic purity of Ge should not affect this figure of merit.

Discussions with the members of the IST group regarding the performances of their quantum dots fabricated on these samples will provide a feedback useful to understand the impact of these characterization values on the stability of qubits.

The new *body gate* design is an important improvement, since now more stable measurements will be available, meaning more reliable percolation

density values. This design is possible because is now confirmed that the oxide layer activates the conduction at its maximum.

In order to improve the efficiency of electrical characterizations L-NESS started to develop an internal fabrication process for Hall bars.

References

[1]   M. Veldhorst et al. "A two-qubit logic gate in silicon". In: *Nature* 526.7573 (2015), pp. 410–414.

[2]   M. Veldhorst et al. "Silicon CMOS architecture for a spin-based quantum computer". In: *Nature Communications* 8 (2017), p. 1766.

[3]   Pascale Senellart, Glenn Solomon, and Andrew White. "High-performance semiconductor quantum-dot single-photon sources". In: *Nat. Nanotechnol.* 12 (2017), pp. 1026–1039.

[4]   Mete Atatüre et al. "Material platforms for spin-based photonic quantum technologies". In: *Nat. Rev. Mater.* 3 (2018), pp. 38–51.

[5]   T. F. Watson et al. "A programmable two-qubit quantum processor in silicon". In: *Nature* 555.7698 (2018), pp. 633–637.

[6]   G. Isella et al. "Low-energy plasma-enhanced chemical vapor deposition for strained Si and Ge heterostructures and devices". In: *Solid State Electron.* 48.8 (2004), pp. 1317–1323.

[7]   Daniel Loss and David P. DiVincenzo. "Quantum computation with quantum dots". In: *Phys. Rev. A* 57.1 (1998), pp. 120–126.

[8]   D. Sabbagh et al. "Quantum Transport Properties of Industrial ^{28}Si/^{28}SiO$_2$". In: *Phys. Rev. App.* 12.1 (2019), p. 014013.

[9]   J. R. Petta et al. "Coherent Manipulation of Coupled Electron Spins in Semiconductor Quantum Dots". In: *Science* 309.5744 (2005), pp. 2180–2184. ISSN: 0036-8075. DOI: 10.1126/science.1116955. eprint: https://science.sciencemag.org/content/309/5744/2180.full.pdf.

[10]   Lada Vukušić et al. "Single-Shot Readout of Hole Spins in Ge". In: *Nano Lett.* 18.11 (2018), pp. 7141–7145.

[11]   Hannes Watzinger et al. "A germanium hole spin qubit". In: *Nature Communications* 9 (2018), p. 3902.

[12]   N. W. Hendrickx et al. "Gate-controlled quantum dots and superconductivity in planar germanium". In: *Nature Communications* 9 (2018), p. 2835.

[13]   Amir Sammak et al. "Shallow and Undoped Germanium Quantum Wells: A Playground for Spin and Hybrid Quantum Technology". In: *Adv. Funct. Mater.* 2019 (2019), p. 1807613.

[14]   Alessandro Crippa et al. "Electrical Spin Driving by *g*-Matrix Modulation in Spin-Orbit Qubits". In: *Phys. Rev. Lett.* 120.13 (2019), p. 137702.

[15] Andrea Hofmann et al. "Assessing the potential of Ge/SiGe quantum dots as hosts for singlet-triplet qubits". In: *arXiv.org e-Print archive* cond-mat (2019), arXiv:1910.05841.

[16] Yuhki Itoh, Shinji Hatakeyama, and Katsuyoshi Washio. "Structural transition in Ge growth on Si mediated by sub-monolayer carbon". In: *Thin Solid Films* (2014), in press.

[17] D. Laroche et al. "Magneto-transport analysis of an ultra-low-density two-dimensional hole gas in an undoped strained Ge/SiGe heterostructure". In: *Appl. Phys. Lett.* 108.23 (2016), p. 233504.

[18] T. M. Lu et al. "Capacitively induced high mobility two-dimensional electron gas in undoped $Si/Si_{1-x}Ge_x$ heterostructures with atomic-layer-deposited dielectric". In: *Appl. Phys. Lett.* 90.18 (2007), p. 182114.

[19] S. Sarkozy et al. "Low temperature transport in undoped mesoscopic structures". In: *Appl. Phys. Lett.* 94.17 (2009), p. 172105.

[20] M. P. Lilly et al. "Resistivity of Dilute 2D Electrons in an Undoped GaAs Heterostructure". In: *Phys. Rev. Lett.* 90.5 (2003), p. 056806.

[21] S. Marchionna et al. "Defect imaging of SiGe strain relaxed buffers grown by LEPECVD". In: *Mat. Sci. Semicond. Process.* 9.4–5 (2006), pp. 802–805.

[22] M. Lodari et al. "Light effective hole mass in undoped Ge/SiGe quantum wells". In: *Phys. Rev. B* 100.4 (2019), p. 041304.

[23] M. Bonfanti et al. "Direct-gap related optical transitions in Ge/SiGe quantum wells with Ge-rich barriers". In: *Physica E* 41.6 (2009), pp. 972–975.

[24] D. Chrastina. "Transport in Silicon-Germanium Heterostructures". PhD thesis. University of Warwick, U.K., 2001.

[25] D. Rideau et al. "Strained Si, Ge, and $Si_{1-x}Ge_x$ alloys modeled with a first-principles-optimized full-zone $k.p$ method". In: *Phys. Rev. B* 74.19 (2006), p. 195208.

[26] Y. Takeda and T. Pearsall. "Failure of Matthiessen's rule in the calculation of carrier mobility and alloy scattering effects in Ga0.47In0.53As". In: *Electronics Letters* 17 (1981), pp. 573–574.

[27] G. Dresselhaus, A. F. Kip, and C. Kittel. "Cyclotron Resonance of Electrons and Holes in Silicon and Germanium Crystals". In: *Phys. Rev.* 98.3 (1955), pp. 368–384.

[28] R. J. P. Lander et al. "On the low-temperature mobility of holes in gated oxide Si/SiGe heterostructures". In: *Semicond. Sci. Technol.* 12.9 (1997), pp. 1064–1071.

[29] J. H. Davies. *The Physics of Low-Dimensional Semiconductors*. Cambridge University Press, 1998.

[30] P. T. Coleridge, R. Stoner, and R. Fletcher. "Low-field transport coefficients in GaAs/Ga$_{1-x}$Al$_x$As heterostructures". In: *Phys. Rev. B* 39.2 (1989), pp. 1120–1124.

[31] S. Madhavi, V. Venkataraman, and Y. H. Xie. "High room-temperature hole mobility in Ge$_{0.7}$Si$_{0.3}$/Ge/Ge$_{0.7}$Si$_{0.3}$ modulation-doped heterostructures". In: *J. Appl. Phys.* 89.4 (2001), pp. 2497–2499.

[32] B. Rössner et al. "Scattering mechanisms in high-mobility strained Ge channels". In: *Appl. Phys. Lett.* 84.16 (2004), pp. 3058–3060.

[33] P. T. Coleridge. "Small-angle scattering in two-dimensional electron gases". In: *Phys. Rev. B* 44.8 (1991), pp. 3793–3801.

[34] M. J. Kearney and A. I. Horrell. "The effect of alloy scattering on the mobility of holes in a Si$_{1-x}$Ge$_x$ quantum well". In: *Semicond. Sci. Technol.* 13.2 (1998), pp. 174–180.

[35] L. A. Tracy et al. "Observation of percolation-induced two-dimensional metal-insulator transition in a Si MOSFET". In: *Phys. Rev. B* 79.23 (2009), p. 235307.

[36] S. Das Sarma and E. H. Hwang. "Charged Impurity-Scattering-Limited Low-Temperature Resistivity of Low-Density Silicon Inversion Layers". In: *Phys. Rev. Lett.* 83.1 (1999), pp. 164–167.

[37] S. Das Sarma and E. H. Hwang. "Metallicity and its low-temperature behavior in dilute two-dimensional carrier systems". In: *Phys. Rev. B* 69.19 (2004), p. 195305.

[38] Mario Lodari et al. "Low percolation density and charge noise with holes in germanium". In: *Mater. Quantum Technol.* 1.1 (2021), p. 011002.

[39] D. Chrastina et al. "LEPECVD – a Production Technique for SiGe MOSFETs and MODFETs". In: *Materials for Information Technology*. Ed. by Ehrenfried Zschech, Caroline Whelan, and Thomas Mikolajick. Springer, 2005, pp. 17–29.

[40] Bernard S. Meyerson, Kevin J. Uram, and Francoise K. LeGoues. "Cooperative growth phenomena in silicon/germanium low-temperature epitaxy". In: *Appl. Phys. Lett.* 53.25 (1988), pp. 2555–2557.

[41] J. M. Hartmann et al. "SiGe growth kinetics and doping in reduced pressure-chemical vapor deposition". In: *J. Cryst. Growth* 236.1–3 (2002), pp. 10–20.

[42] Maurizio Rondanini et al. "An experimental and theoretical investigation of a magnetically confined dc plasma discharge". In: *J. Appl. Phys.* 104.1 (2008), p. 013304.

[43] W. A. Beck and J. R. Anderson. "Determination of electrical transport properties using a novel magnetic field-dependent Hall technique". In: *J. Appl. Phys.* 62.2 (1987), pp. 541–554.

[44] J. W. McClure. "Field Dependence of Magnetoconductivity". In: *Phys. Rev.* 101.6 (1956), pp. 1642–1646.

[45] D. Chrastina, J. P. Hague, and D. R. Leadley. "Application of Bryan's algorithm to the mobility spectrum analysis of semiconductor devices". In: *J. Appl. Phys.* 94.10 (2003), pp. 6583–6590.

[46] S. M. Girvin. "The Quantum Hall Effect: Novel Excitations And Broken Symmetries". In: *Aspects topologiques de la physique en basse dimension. Topological aspects of low dimensional systems. Les Houches - Ecole dâ€™Ete de Physique Theorique.* Ed. by Comtet A. et al. Vol. 69. Springer, Berlin, Heidelberg, 1999.

[47] Zhouquan Yuan. "Quantum transport in spatially modulated two-dimensional electron and hole systems". PhD thesis. Rice University, Houston, 2009.

[48] Harald Ibach and Hans Lüth. *Solid-State Physics: An Introduction to Principles of Materials Science.* Springer-Verlag Berlin and Heidelberg GmbH, 2009.

[49] David Tong. "The Quantum Hall Effect". In: *arXiv.org e-Print archive* hep-th (2016), arXiv:1606.06687.

[50] A. Isihara and L. Smrčka. "Density and magnetic field dependences of the conductivity of two-dimensional electron systems". In: *J. Phys. C. Solid State Phys.* 19.34 (1986), pp. 6777–6789.

[51] Manna Kumari Mishra et al. "On the Determination of Electron Effective Mass in 2DEGs in Gallium Nitride HEMT Structures". In: *Physics of Semiconductor Devices. Environmental Science and Engineering.* Ed. by V. Jain and A. Verma. Springer, 2014, pp. 99–101.

[52] B. Rößner, G. Isella, and H. von Känel. "Effective mass in remotely doped Ge quantum wells". In: *Appl. Phys. Lett.* 82.5 (2003), pp. 754–756.

[53] F. A. Stevie et al. "Boron contamination of surfaces in silicon microelectronics processing: Characterization and causes". In: *J. Vac. Sci. Technol. A* 9.5 (1991), pp. 2813–2816.

[54] X. Mi et al. "Magnetotransport studies of mobility limiting mechanisms in undoped Si/SiGe heterostructures". In: *Phys. Rev. B* 92.3 (2015), p. 035304.

[55] Oliver A. Dicks et al. "The origin of negative charging in amorphous Al_2O_3 films: the role of native defects". In: *Nanotechnology* 30.20 (2019), p. 205201.

[56] Floriano Traversi. "Caratterizzazione delle proprietà di trasporto in strutture p-MOD a base di Si/Ge". MA thesis. Politecnico di Milano, 2006.

[57] Y. H. Xie et al. "Very high mobility two-dimensional hole gas in $Si/Ge_xSi_{1-x}/Ge$ structures grown by molecular beam epitaxy". In: *Appl. Phys. Lett.* 63.16 (1993), pp. 2263–2264.

[58] M. Myronov et al. "Temperature dependence of transport properties of high mobility holes in Ge quantum wells". In: *J. Appl. Phys.* 97.8 (2005), p. 083701.

[59]   K. Sawano et al. "Compressive strain dependence of hole mobility in strained Ge channels". In: *Appl. Phys. Lett.* 87.19 (2005), p. 192102.